Snapshot of in-cell protein contact sites reveals new host factors and hijacking of paraspeckles during influenza A virus infection

Iuliia Kotova[1,2], Lars Mühlberg[6], Konstantin Gilep[1,2], Dingquan Yu[1,2], Daniel Ziemianowicz[1,2], Stephanie Stanelle-Bertram[4], Sebastian Beck[4], Kyungmin Baeg[3], Olivier Duss[3], Gülsah Gabriel[4,5], Fan Liu[6*], Boris Bogdanow[6,7*], Jan Kosinski[1,2,3*]

[1] European Molecular Biology Laboratory Hamburg, Notkestraße 85, 22607 Hamburg, Germany

[2] Centre for Structural Systems Biology (CSSB), Notkestraße 85, 22607 Hamburg, Germany

[3] Molecular Systems Biology Unit, European Molecular Biology Laboratory, Meyerhofstrasse 1, Heidelberg 69117, Germany

[4] Research Department Viral Zoonoses – One Health, Leibniz Institute of Virology (LIV), Martinistraße 52, 20251 Hamburg, Germany

[5] Research Center for Emerging Infections and Zoonoses, University of Veterinary Medicine Hannover, Buenteweg 17, 30559 Hannover, Germany

[6] Department of Structural Biology, Leibniz-Forschungsinstitut für Molekulare Pharmakologie (FMP), Berlin, Germany

[7] Institute of Virology, Charité—Universitätsmedizin Berlin, Freie Universität Berlin and Humboldt-Universität zu Berlin, Berlin Institute of Health, Berlin, Germany

[*] Correspondence: jan.kosinski@embl.de (J.K), boris.bogdanow@charite.de (B. B.), FLiu@fmp-berlin.de (F.L)

Summary

Influenza A virus (IAV) exploits the host cellular machinery to facilitate its replication, yet many host-IAV interactions remain unexplored in the cellular context. Detailed information about interacting domains is also largely lacking. To address this, we employed in-cell cross-linking mass spectrometry (XL-MS) to capture a vast network of protein-protein contact sites within IAV-infected human cells. This approach uncovered previously unrecognised host factors, delineated steps of the hemagglutinin maturation pathway, and revealed that IAV progressively disrupts

paraspeckles. We further found that paraspeckle disruption is mediated by NP and NS1 interactions, PA-X activity, and inhibition of RNA polymerase II, thereby liberating RNA-binding proteins that enhance viral replication. Our work advances the understanding of IAV manipulation of host cellular processes and demonstrates the utility of in-cell XL-MS for comprehensive mapping of host-pathogen interactomes and infection pathways.

Highlights

- In-cell cross-linking maps protein contact sites in IAV infection
- Steps of the hemagglutinin maturation pathway can be delineated by cross-linking
- IAV proteins interact with components of paraspeckles
- IAV disrupts paraspeckles releasing pro-viral host factors

Keywords

Influenza virus, protein-protein interactions, host-pathogen interactions, cross-linking mass spectrometry, host factors, paraspeckles, NEAT1, hemagglutinin, LAT1

Introduction

Influenza A virus (IAV) remains a major global health threat, causing substantial annual morbidity and mortality[1]. The viral replication cycle culminates in the biogenesis of viral progeny within infected host cells, driven by protein-protein interactions (PPIs) between viral and host proteins[2]. The IAV genome consists of eight gene segments encoding up to 14 proteins, depending on the strain[2]. These proteins engage in dynamic interactions that form and dissociate depending on the stage of infection and are often confined to specific cellular compartments and organelles. Thus, understanding host-IAV PPIs in their native cellular and spatial context is essential for elucidating viral strategies of host manipulation and identifying therapeutic targets.

One of the most prominent examples of the importance of subcellular context in defining IAV-host PPIs is viral RNA (vRNA) synthesis. This process is confined to the nucleus and is catalysed by the viral RNA-dependent RNA polymerase complex (RdRp), composed of PA, PB1, and PB2 proteins. vRNA synthesis is further embedded in the spatial context of the viral ribonucleoproteins (vRNPs), composed of

RdRp and viral vRNA wrapped around NP protein filament[2]. Moreover, assembly of RdRp, along with transcription and replication, is facilitated by the recruitment of additional host factors[3–6].

Similarly, nuclear vRNA processing is modulated by context-specific PPIs between viral proteins, such as NS1 and NP, and host RNA-binding proteins[7,8]. These proteins remodel sub-nuclear compartments, such as nuclear speckles, which are essential for splicing of IAV mRNA[9]. Furthermore, the viral PA-X nuclease, expressed from an alternative reading frame of PA[10], degrades nuclear host transcripts[11,12], which are known to organise subnuclear compartments in uninfected cells[13]. However, how context-specific protein and RNA interactions in infected cells influence subnuclear compartments and whether this impacts replication remains poorly understood.

The importance of context-specific PPIs within dynamic macromolecular assemblies and organelles extends beyond the nucleus. Newly synthetised vRNPs are exported from the nucleus by nuclear export factors, a process mediated by viral proteins M1[14] and NEP[15]. Consequently, vRNPs are trafficked through the cytoplasm to the plasma membrane via an interaction with host RAB11A protein[16] at the endoplasmic reticulum (ER), which undergoes architectural reorganisation during infection[17]. In parallel, surface viral glycoproteins hemagglutinin (HA) and neuraminidase (NA) are synthesised in the ER, glycosylated in the Golgi, and trafficked to the plasma membrane[18], involving extensive interactions with the cellular machinery for glycoprotein maturation. Ultimately, glycoproteins, vRNPs, M1 and the ion channel M2 converge to assemble into viral particles that bud from the plasma membrane.

Despite the clear importance of subcellular and infection contexts in shaping functionally relevant PPIs during IAV infection, systematic data on IAV-host PPIs in these native contexts is lacking. Instead, methods such as affinity purification mass spectrometry (AP-MS) and yeast-two-hybrid (Y2H) assays have identified many IAV-host PPIs[19–28], but have relied on cell lysates and often non-infected cells, disrupting native cellular architecture and dynamic macromolecular assemblies. Moreover, these methods do not provide insights into interaction sites and structures of complexes, which have barely been characterised at atomic resolution for IAV host-pathogen PPIs.

Cross-linking mass spectrometry (XL-MS) is a powerful approach to address these challenges and knowledge gaps as it allows capturing protein interactions from intact cells and provides residue-to-residue connections of interaction protein pairs. Here, we applied in-cell cross-linking mass spectrometry XL-MS[29] using disuccinimidyl sulfoxide (DSSO) cross-linker combined with functional and structural analysis to map IAV PPIs within infected human lung epithelial cells. This approach identified cross-links between IAV and human proteins in their native context, defining residue-residue pairs in close proximity (within 40 Å based on the distance constraint of DSSO) due to direct or indirect interactions, hereafter referred to as contact sites.

Integrating XL-MS data with functional screens, we identified novel host factors, including contributors to HA maturation in the ER/Golgi and the LAT1 amino acid transporter as an M2 interactor. Following observations of extensive cross-links to host RNA-binding proteins, we demonstrated that IAV disrupts paraspeckles — membraneless nuclear organelles. Mechanistically, we propose that NP and NS1 interactions with paraspeckle protein components, degradation of non-coding RNA NEAT1_2 by PA-X, and RNA Pol II inhibition collectively drive this process. This disruption liberates RNA-binding proteins that facilitate vRNA synthesis and replication.

Our findings provide a snapshot of IAV-host contact sites in cells, offering global spatial and structural insights into viral manipulation of the host cellular machinery.

Results

Mapping IAV-human contact sites using in-cell cross-linking

To map PPIs and their contact sites in IAV-infected cells, we applied XL-MS-based structural host-virus interactome profiling (SHVIP) (Figure 1A). SHVIP mitigates the inherent sensitivity limitation of conventional in-cell XL-MS by combining XL-MS and bio-orthogonal labelling with unnatural amino acids for the selective enrichment of newly synthesised viral proteins[29].

To apply SHVIP to IAV, we optimised the labelling to enrich the viral proteome while preserving the physiological context of infected cells (Figure S1A-E). Previous bio-orthogonal amino acid labelling studies showed that dominant IAV protein synthesis begins a few hours post-infection and slows during later stages[30]. We timed the cross-

linking and labelling scheme to capture the late infection stage (see Methods and Figure S1C-F), during which vRNP export, cytoplasmic genome transport, and virion assembly occur at the plasma membrane[31]. Additionally, we confirmed that L-HPG labelling did not affect cell viability or infection progression (Figure S1G-I), ensuring minimal disruption to productive IAV infection.

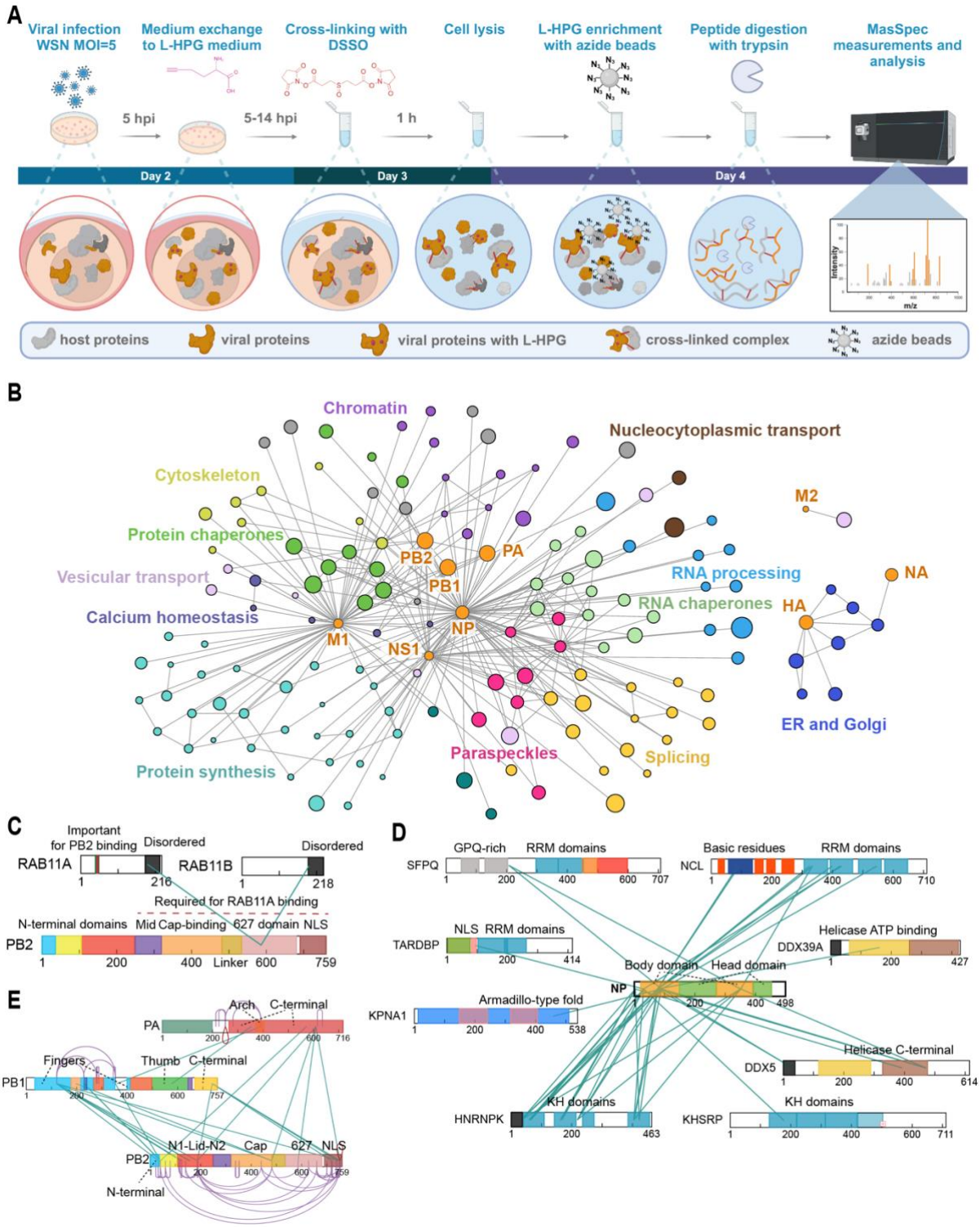

Figure 1 In-cell cross-linking during influenza A virus infection.

(A) In-cell cross-linking using SHVIP. IAV-infected cells are labelled with HPG from 5 to 14 hpi, followed by DSSO cross-linking. After quenching, L-HPG-incorporated

proteins are enriched via click chemistry, digested with trypsin, and cross-links are analysed by MS. *Created in BioRender.* https://BioRender.com/g57m779

(B) Virus-centric cross-linking network at a 2% FDR threshold. Viral proteins are shown in orange, and host proteins are coloured by their functional category. Only host proteins linked to viral proteins are shown with names omitted for clarity. The network including host names is shown in Figure S2.

(C) Interaction between PB2 and RAB11A/B, consistent with the established binding domain of PB2. Interlinks are shown in green, while intralinks are omitted for clarity.

(D) Cross-links between NP and established host factors involved in influenza virus infection. Colour shading represents distinct structural domains, with names shown only for those forming cross-links for clarity. Interlinks are shown in green, while intralinks are omitted for clarity.

(E) Cross-links between subunits of vRdRp. Interlinks are shown in green, while Intralinks in violet.

To confirm that SHVIP efficiently enriches the viral proteome, we compared host and viral protein abundance in enriched samples versus input aliquots across three replicates. Viral proteins were, on average, ten times more abundant in enriched samples (Figure S1I-L). Likewise, proteomic XL-MS analysis showed that viral protein pairs and cross-links were detected 2-10 times more frequently in enriched samples (Figure S1M-O). Pairwise reproducibility across replicates (47% on average) (Figure S1P-R) matched previous large-scale XL-MS studies[32] and the SHVIP HSV-1 dataset[29].

Extensive *in-cell* cross-linking network

We analysed the combined raw data from three biological SHVIP replicates, applying a consecutive 2% FDR threshold for cross-link spectrum match (CSM), residue-pair (Table S1A) and PPI levels (Table S1B). This dataset included 13201 unique residue-pair cross-links (Table S1C) originating from 1961 proteins. In particular, 111 viral-viral cross-links and 877 viral-host cross-links were identified. These involve nine viral proteins, 141 host proteins, and 200 viral-host protein pairs (Table S1D, Figure 1B).

Of the viral-host interactions, at least 50 protein pairs involved host proteins known to bind viral proteins (Table S2, Figure S2). We also found cross-links to host factors known to function in the IAV infection cycle, such as RAB11A (Figure 1C), KHSRP[33] and TDP-43(TARDBP)[34] (Figure 1D), ANP32A and ANP32B[35], nucleosomes[36,37], microtubules[38], and chaperonins[39].

The captured interactome is enriched for functional Gene Ontology (GO) terms related to gene expression, RNA processing, splicing, and transport, response to unfolded proteins, protein synthesis, ribosome biogenesis, chromatin organisation, and regulation of calcium homeostasis and phosphorylation (Figure 1B, Figure S2, Table S3). The interacting proteins localise to both nuclear and cytoplasmic compartments, with notable enrichment in the nucleolus, cytoskeleton, and vesicles (Table S3). Many of these enriched spatial and functional categories align with previous influenza virus PPI studies[19,40].

A unique advantage of the XL-MS over AP-MS and Y2H is that cross-links provide distance constraints to corroborate protein structures or guide structural modelling[41]. Mapping host-host cross-links onto structures from the Protein Data Bank (PDB) showed that 93% of the C_α-C_α distances between cross-linked residues fall within the DSSO cross-linker constraint of 40 Å (Figure S3). For viral complexes such as RdRp, cross-link satisfaction rates are difficult to calculate due to conformational and oligomeric heterogeneity[42,43]. Nonetheless, the cross-linking pattern of RdRp (Figure 1E) aligns with the cross-linking pattern observed for purified RdRp[43]. For IAV-host interactions, no structures available in the PDB contained cross-links that connected the structurally resolved regions of IAV and human proteins, underscoring the challenges of capturing these interactions structurally. Attempts to model the IAV-human interactions using AlphaFold2-multimer[44,45], AlphaFold3[46] and AF3x[47] resulted in very few well-scoring predictions for cross-linked pairs (Figure S5, Table S4), likely due to the reliance of AlphaFold on co-evolutionary signals and sequence pairing from the same species, which is not achievable in host-pathogen systems[45].

Overall, the substantial overlap of the identified cross-links with functional host protein categories, known host factors, PPIs characteristic of IAV infection, and AlphaFold models, demonstrates that SHVIP delivers a structurally informative interactome at the virus-host interface.

Cross-linking network and siRNA screening reveal new host factors and functional hypotheses

To demonstrate that our cross-linking network identifies novel host factors in IAV infection and generates a wealth of functional hypotheses, we performed an siRNA-mediated loss-of-function screen targeting selected cross-linked host proteins (Figure 2A). We prioritised host proteins with at least three cross-links to viral proteins, excluding well-studied host factors. Additionally, we included six host proteins with fewer cross-links—ERP29, LMAN2, EEF1A1, SET, SSB, and RALY—due to their roles in nucleic acid metabolism, gene expression regulation, and ER localisation. We also included SLC3A2 as the sole identified M2 interactor, and RAB11A (a known IAV dependency factor) as a positive control. IAV infection efficiency in siRNA-treated cells was quantified using a luciferase assay[48] (Figure 2A, Figure S4A-B). RAB11A reduced viral replication by ~10-fold (Figure 2B), which is consistent with previous reports[31,49] and validates our assay. In addition, knockdown of ribosomal 60S subunit proteins RPL35 (cross-linked to NS1, M1, and NP) and RPL10A (cross-linked to M1) significantly reduced viral replication, whereas knockdown of other ribosomal proteins had no effect on viral titres, suggesting that these interactions have a specific function (Figure 2B, Figure S4A-B). These findings are consistent with the role of NS1 in regulating protein translation[50] and suggest additional roles for IAV interactions with the translational machinery.

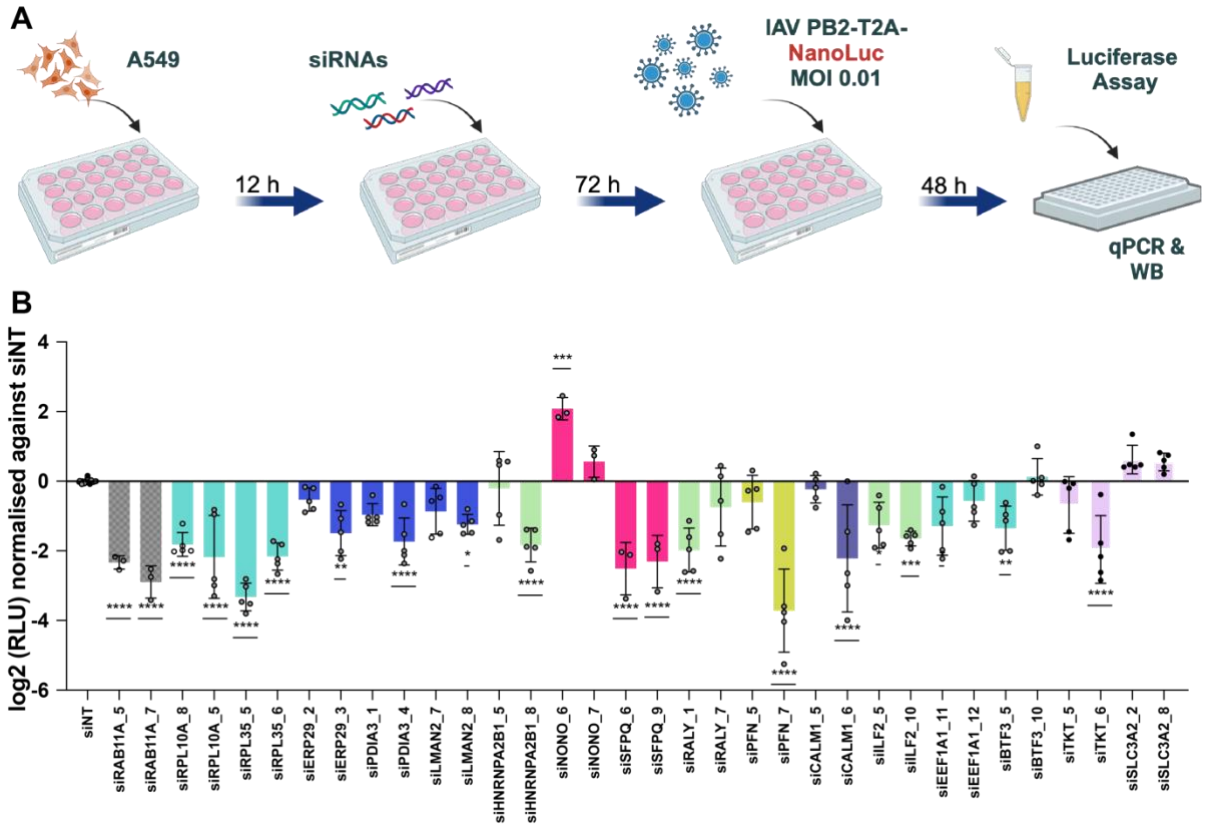

Figure 2. Impact of siRNA-mediated knockdown on IAV infection.

(A) Schematic of luciferase assay: A549 cells were transfected with siRNAs and at 72 hpt (hours post-transfection), cells were infected with recombinant WSN virus expressing PB2-T2A-NanoLuc. After 48 hours, luciferase activity was measured (Figure S4C-D), providing read-out proportional to viral polymerase levels in infected, siRNA-treated cells[52]. Created in BioRender https://BioRender.com/h91s731

(B) Log2-transformed relative luciferase units [Log2 (RLU)] normalised to a non-targeting siRNA control (siNT). Data are represented as mean ± standard deviation (SD) (n = 3 to 5 Statistical significances: *p<0.05, **p<0.01, ***p<0.001, ****p<0.0001 (one-way ANOVA and Dunnett's multiple comparisons test, reference: siNT). See also Figure S4A-B.

We further examined SLC3A2, the knockdown of which caused a small increase but was statistically significant only for one of the two siRNAs (Figure 2B). SLC3A2, as well as its known interactor SLC7A5 (both are components of a dimeric complex, namely the large neutral amino acid transporter (LAT1)[51] cross-linked to M2 with two cross-links at 2% FDR and an additional cross-link at 5% FDR (Table S1E-G). All cross-links are consistent with the orientation of LAT1 and M2 across the membrane

(Figure 3A). LAT1 is essential for amino acid uptake and mTORC1 activation, processes supporting cell growth and survival[51,52]. Knockdown of either LAT1 subunit increased IAV infection in A549 cells (Figure 3B). To validate the interaction, we performed co-IPs from infected cells against SLC3A2 and SLC7A5. M2 co-immunoprecipitated with both LAT1 subunits (Figure S6A). Additionally, we performed an AP-MS experiment in infected cells comparing pull-down against SLC7A5 and M2 to isotype-matched specificity controls. This revealed the mutual enrichment of M2 and SLC7A5 (Figure 3C, Figure S6B). Co-localisation of M2 and LAT1 at the plasma membrane was observed in A549 (Figure 3D-F) and primary cell lines (Figure S6D-H), indicating that the interaction between M2 and LAT1 subunits occurs at cellular membranes, with potential roles in regulating amino acid transport or M2 localisation.

These findings establish SHVIP as a robust approach for identifying host proteins with critical roles in IAV infection. Beyond these examples, infection was affected by the knockdown of several host proteins linked to ER function and paraspeckles, which are discussed in the following sections.

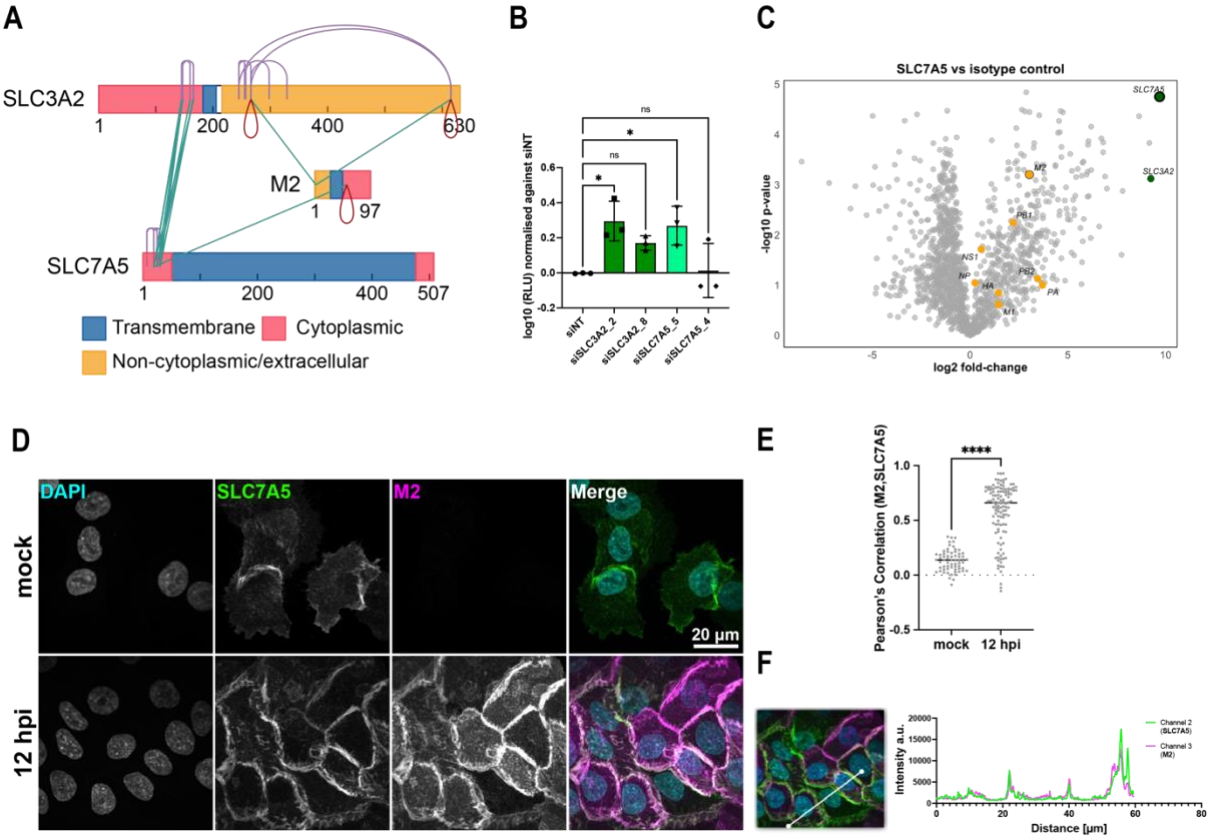

Figure 3. Analysis of M2-LAT1 interaction

(A) Cross-linking network of M2 and LAT1

(B) Log(RLU) normalised to siNT. Data are represented as mean ± SD (n = 3), with individual experiment means shown as circles. Statistical analysis was performed using ordinary one-way ANOVA. Statistical significance: *p<0.05, **p<0.01, ***p<0.001, ****p<0.0001. siSLC3A2 is replicated from Figure 2B.

(C) Volcano plots showing fold-change (log2) versus significance (-log10 p-value) for SLC7A5 versus isotype control. Viral proteins are depicted in orange, SLC7A5 and SLC3A2 – in green.

(D) Maximum intensity projection (MaxIP) of confocal images from A549 cells infected with WSN (Multiplicity of infection (MOI) 3) or mock at 12 hpi. Cells were stained for SLC7A5 (green), M2 (magenta), and nuclei (DAPI, cyan). Scale bars, 20 µm.

(E) Pearson's correlation coefficient quantification of SLC7A5 and M2 colocalisation in membrane regions. Analysis was performed in mock-infected cells (n = 64) and WSN-infected cells at 12 hpi (n = 119). Statistical significance was determined using the Mann-Whitney test (****p<0.0001).

(F) Representative plane and intensity profile showing the co-localisation of SLC7A5 and M2 in A549 cells at 12 hpi.

The steps of the early secretory pathway of HA mapped by cross-linking

We found HA cross-linked to several ER and Golgi apparatus proteins, with all cross-links supporting the same protein orientations across the membrane (Figure 4A). HA is synthesised in the ER and undergoes folding, N-linked glycosylation, and processing in the ER and Golgi before export to the plasma membrane[53–56]. Examining the ER and Golgi proteins cross-linked to HA indicated that the XL-MS data can be used to reconstruct the sequential steps of the HA secretory pathway (Figure 4B).

The first step of the pathway is recapitulated by cross-links from HA to calnexin (CANX) and calreticulin (CALR), key chaperones in glycoprotein folding and trafficking[57], agreeing with the demonstrated role of CANX and CALR in HA processing[58–60]. Cross-links localised to HA stalk and head domains, aligning with AlphaFold3 models of CALR bound to N-glycans on HA (Figure 4B). HA also cross-linked with protein disulfide isomerase PDIA3, supporting its role in the disulfide bond formation of HA[61,62], as well as with protein disulfide isomerase TMX1 and an ER chaperone ERP29[63], not previously linked to HA maturation. Supporting the

involvement of PDIA3 and ERP29 in the HA pathway, the knockdown of these proteins in our initial siRNA screen reduced IAV infection (Figure 2B).

Further along the pathway, HA cross-linked with ERGIC-53 and VIP36 (also known as LMAN1 and LMAN2, respectively, with LMAN2 only detected in the non-stringently filtered cross-link list, Table S1E-G), lectins involved in glycoprotein trafficking[64–67]. In support of the role of VIP36 in the HA maturation pathway, VIP36 knockdown significantly reduced IAV infection (Figure 2B). While ERGIC-53 supports glycoprotein production in other viruses[66], VIP36 has not yet been implicated in influenza infection. The interaction of ERGIC-53 and VIP36 with HA may facilitate the transport of HA through the Golgi apparatus and possibly aid in its sorting to the plasma membrane. HA also cross-linked with Beta-1,4-galactosyltransferase 1 (B4GALT1), which resides in the Golgi, suggesting B4GALT1 involvement in further processing of HA, and TM9SF2, a protein implicated in Golgi and endosomal sorting[68–72]. This interaction could explain that TM9SF2 overexpression inhibits IAV infection[73], suggesting a potential antiviral role of TM9SF2.

In summary, these results suggest a pathway in which HA interacts with CANX, CALR, ERP57, ERP29, and TMX1 in the ER, traffics via ERGIC-53 and VIP36, and undergoes further processing by B4GALT1 in the Golgi, possibly regulated by TM9SF2 (Figure 4B). This analysis demonstrates that in-cell XL-MS can effectively map infection pathways in their native cellular context, capturing sequential protein interactions with high spatial and functional resolution.

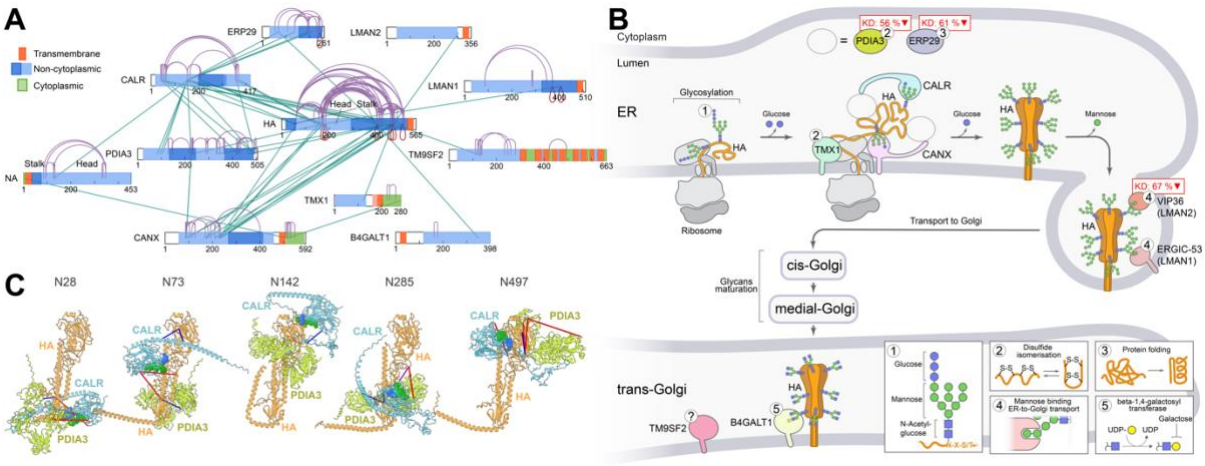

Figure 4. Early secretory pathway of HA mapped by cross-linking.

(A) Cross-linking network of HA. Protein sequences are shown as horizontal bars with structural domains indicated and coloured based on their orientation across the ER membrane.

(B) Early secretory pathway of HA proposed based on the cross-linking and literature data. The % values next to the protein names indicate the impact of the corresponding gene's knockdown on IAV production using a luciferase assay. The inset boxes show the presumed functions of the respective proteins or maturation steps; the question mark indicates an uncharacterised mechanism.

(C) AlphaFold3 models of glycosylated HA monomers bound to CALR and PDIA3, with cross-links mapped. Each model represents a different glycosylation site, with glycan atoms represented as spheres: N-Acetylglucosamine in blue and Mannose in green. Although the models do not recapitulate HA conformational flexibility and increased oligomeric states during processing, these conceptual models illustrate how cross-links align with CALR-PDIA3 binding to HA glycosylation sites. Cross-links connecting residues within a Cα-Cα distance of ≤30 Å are coloured blue, those between 30–40 Å, a threshold taking protein flexibility into account, are coloured magenta, and those longer than 40 Å are coloured red.

IAV proteins interact with paraspeckles and disrupt their integrity

SHVIP identified cross-links from two viral proteins (NP and NS1) to 14 host proteins that are components of paraspeckles (Figure 5A). Paraspeckles are membraneless organelles in the nucleus that are built around long non-coding RNA NEAT1_2, which

is essential for their structural integrity (Figure 5B)[74–79]. The DBHS (Drosophila behaviour, human splicing) family proteins – NONO, SFPQ, and PSPC1 – form the paraspeckle core. Additional proteins such as FUS, CPSF6, and HNRNPK contribute to paraspeckle structure and function[74,80–83]. Paraspeckles modulate gene expression and may influence viral replication and pathogenesis through interactions with viral components[74,75,84].

In support of our SHVIP data (Figure 5A), prior studies have associated the paraspeckle proteins SFPQ, HNRNPK, HNRNPA1, and RBM14 with the IAV infection cycle[5,7,8,85,86] through interactions with IAV proteins NP and NS1[87–92]. Furthermore, we found that knockdowns of SFPQ and NONO affected IAV infection (Figure 2B). We first performed reciprocal immunoprecipitations to confirm interactions of NP with paraspeckle proteins, including NONO, SPFQ and PSPC1 in HEK293T cells (Figure S7A) and WSN-infected A549 cells (Figure S7B-C). Likewise, NONO AP-MS experiment showed enrichment of NONO cross-linking partners such as SPFQ, PSPC1, as well as viral proteins NS1 and NP (Figure 5C). Similarly, an AP-MS experiment targeting NP showed that proteins cross-linked to NP were overall enriched (Figure 5D). Taken together, the XL-MS and AP-MS data indicate interactions of IAV NP and NS1 with paraspeckle proteins, particularly the core component NONO. Moreover, the overlap between NP, NS1 and NONO interactors (Figure S7D-E) suggests that other paraspeckle proteins may also play a role in the viral replication cycle during IAV infection.

Next, to assess the effects of IAV infection on paraspeckles, we used fluorescence in-situ hybridisation (FISH) to localise and quantify NEAT1_1 and NEAT1_2 in WSN-infected compared to non-infected A549 cells (Figure S7F and Figure 5E). While paraspeckles were present in non-infected cells, their number and NEAT1_2 coefficient of variation (CV), which measures signal heterogeneity independently of the mean (see Methods), progressively decreased during infection to very low levels between 4 and 8 hpi (Figure 5F-G and Figure S7F-G). Moreover, in A549 cells overexpressing mEGFP-NONO and mEGFP-SFPQ, these two proteins co-localised with NEAT1_2 (Figure S7H-K), but redistributed to the nucleoplasm during IAV infection (Video S1).

We then extended our analysis to other common host cell lines and IAV strains. Similar reductions in NEAT1_2 CV (Figure 5F) and paraspeckle numbers (Figure 5G) were

observed in WSN-infected Calu-3 cells (Figure S7L), mouse embryonic fibroblasts (MEFs) (Figure S7M), and Human Bronchial Epithelial Cells (HBEpCs), though with a smaller magnitude likely due to lower infection efficiency (Figure S7N). H1N1/California/pdm09 (Figure S7O-P) and H3N2/Aichi/68 (Figure S7Q-R) strains also reduced NEAT1_2 CV and paraspeckle numbers in A549 and HBEpCs cells (Figure S7S-V). Altogether, the results show that IAV disrupts paraspeckles between 4 and 8 hpi consistently across different cell lines and viral strains.

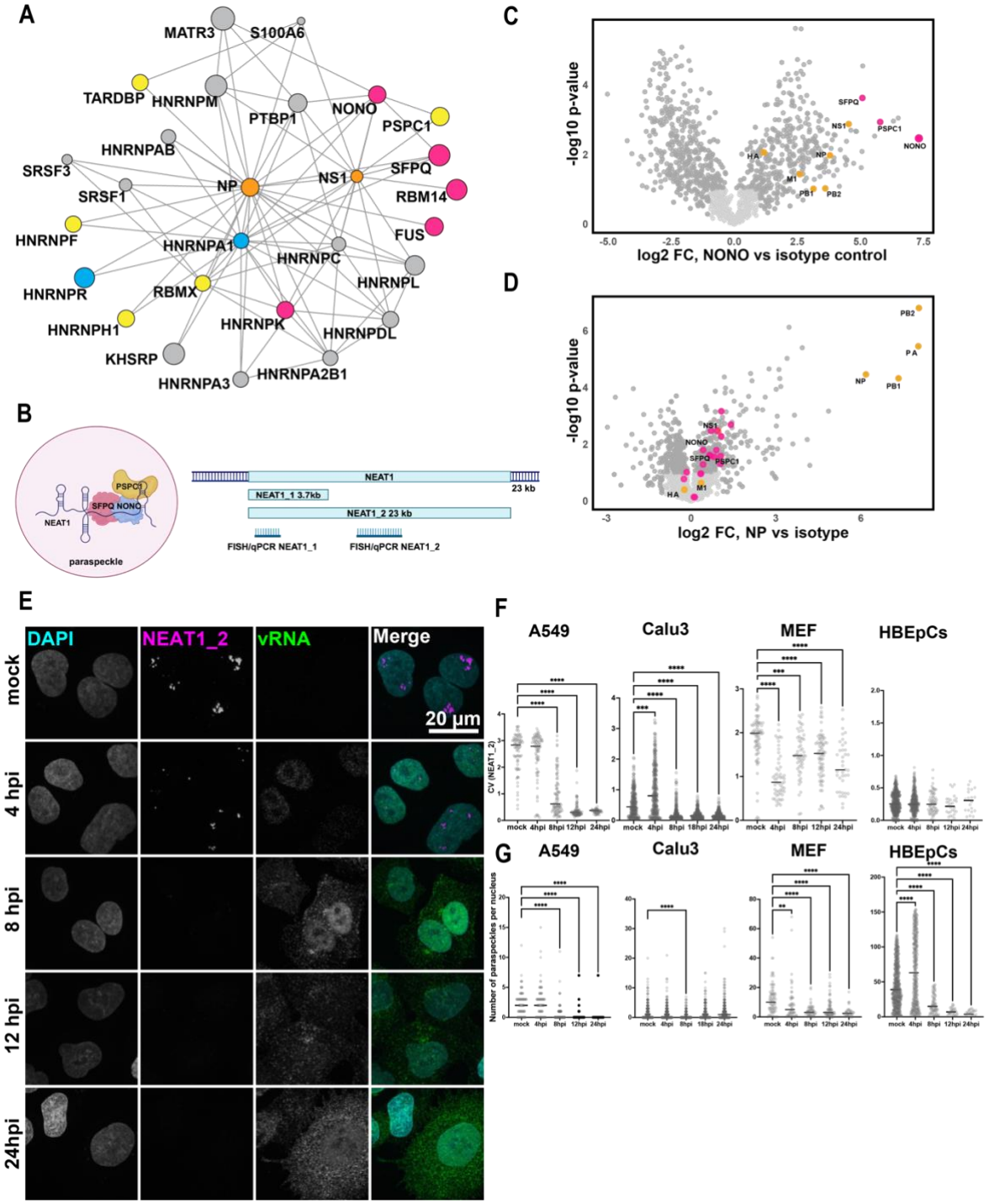

Figure 5. Impact of IAV infection on the paraspeckle formation and NEAT1 expression

(A) Cross-linking network between paraspeckle and viral proteins. Pink – essential for paraspeckle formation, blue – important, yellow – localised to paraspeckles but

dispensable[81], gray – other proteins cross-linked to both paraspeckle and orange - viral proteins.

(B) Paraspeckle structure, showing the interaction between NEAT1 long noncoding RNA and proteins such as SFPQ and NONO (left) and the NEAT1 isoforms, NEAT1_1 and NEAT1_2, and the position of FISH probes/qPCR primers on NEAT1 used in this study (right). Created in bioRender. https://BioRender.com/**b92y974**

(C) AP-MS of NONO versus IgG controls from WSN-infected A549 cells (14 hpi, n=3). NONO and its known interactors are coloured pink and viral proteins - orange.

(D) AP-MS of NP versus IgG controls from WSN-infected A549 cells (14 hpi, n=3). Proteins that were also identified in SHVIP are highlighted. Proteins coloured as in E.

(E) Maximum projection of confocal microscopy images of A549 cells infected with WSN (MOI 3) at 4, 8, and 12 hpi. NEAT1 - magenta, vRNA (PB2 fragment) - green, and DNA (DAPI) - grey.

(F) CV of NEAT1_2 (NEAT1_1 in case of MEF) in the nucleus across different cell lines infected with WSN.

(G) Number of paraspeckles per nucleus across different cell lines infected with WSN.

(F-G) Data are represented as mean + SD. Statistical analysis was performed using ordinary one-way ANOVA. Statistical significance: *$p<0.05$, **$p<0.01$, ***$p<0.001$, ****$p<0.0001$.

To determine whether and which viral proteins contribute to the paraspeckle disruption, we expressed viral proteins NP and NS1 in HEK293T cells. We showed that the individual expression of either NP or NS1 reduces paraspeckle abundance. Co-expression of vRNPs further intensified paraspeckle dissolution compared to NP alone (Figure 6A-C), suggesting that, in addition to NP and NS1, other vRNP components may also affect paraspeckle integrity. We hypothesised that the viral endonuclease PA-X may be responsible, as it is produced via frameshift[11] from the mRNA of the vRNP component PA and its cleavage motif GCUG[11] is present 139 times in NEAT1_2. Indeed, PA-X overexpression in HEK293T cells significantly reduced paraspeckle number (Figure S7D-F), supporting its role in the maintenance of paraspeckle integrity. Complementarily, we assessed the correlation of NEAT1_2

levels and paraspeckle disassembly by qPCR. NEAT1_2 levels were reduced by 50% at 12 hpi in A549 cells and by 15% at 14 hpi in Calu-3 cells (Figure 6J). Paraspeckle disruption occurred earlier (4–8 hpi) in both cell lines (Figure 5F-G, Figure S7L, suggesting that structural disassembly precedes NEAT1 downregulation.

Finally, since paraspeckles depend on an active transcription[84] and viral polymerase is known to bind and inhibit Pol II[93–95], we investigated whether Pol II inhibition disrupts paraspeckles. Indeed, treating non-infected A549 cells with Pol II inhibitor alpha-Amanitin[96] disrupted paraspeckles in a concentration-dependent manner starting 20 hours post-treatment (Figure 6G-I). Since paraspeckle disruption starts within the first 8 hours of infection, this delay suggests that Pol II inhibition contributes to paraspeckle disruption at later infection stages. NONO levels remained stable between mock and infected A549 cells, indicating that paraspeckle disassembly is not caused by NONO downregulation (Figure 6L). Consistently, other essential paraspeckle proteins, such as SFPQ and HNRNPK, also showed no significant reduction in expression. Only FUS, SRSF10 and PSPC1 exhibited a significant increase upon infection (Figure 6M).

Collectively, our findings suggest a three-pronged attack on paraspeckle formation by IAV: NS1- and NP-mediated interactions with paraspeckle protein components, PA-X-dependent degradation of the architectural NEAT1_2 RNA, and possible transcriptional downregulation of NEAT1_2 via Pol II inhibition.

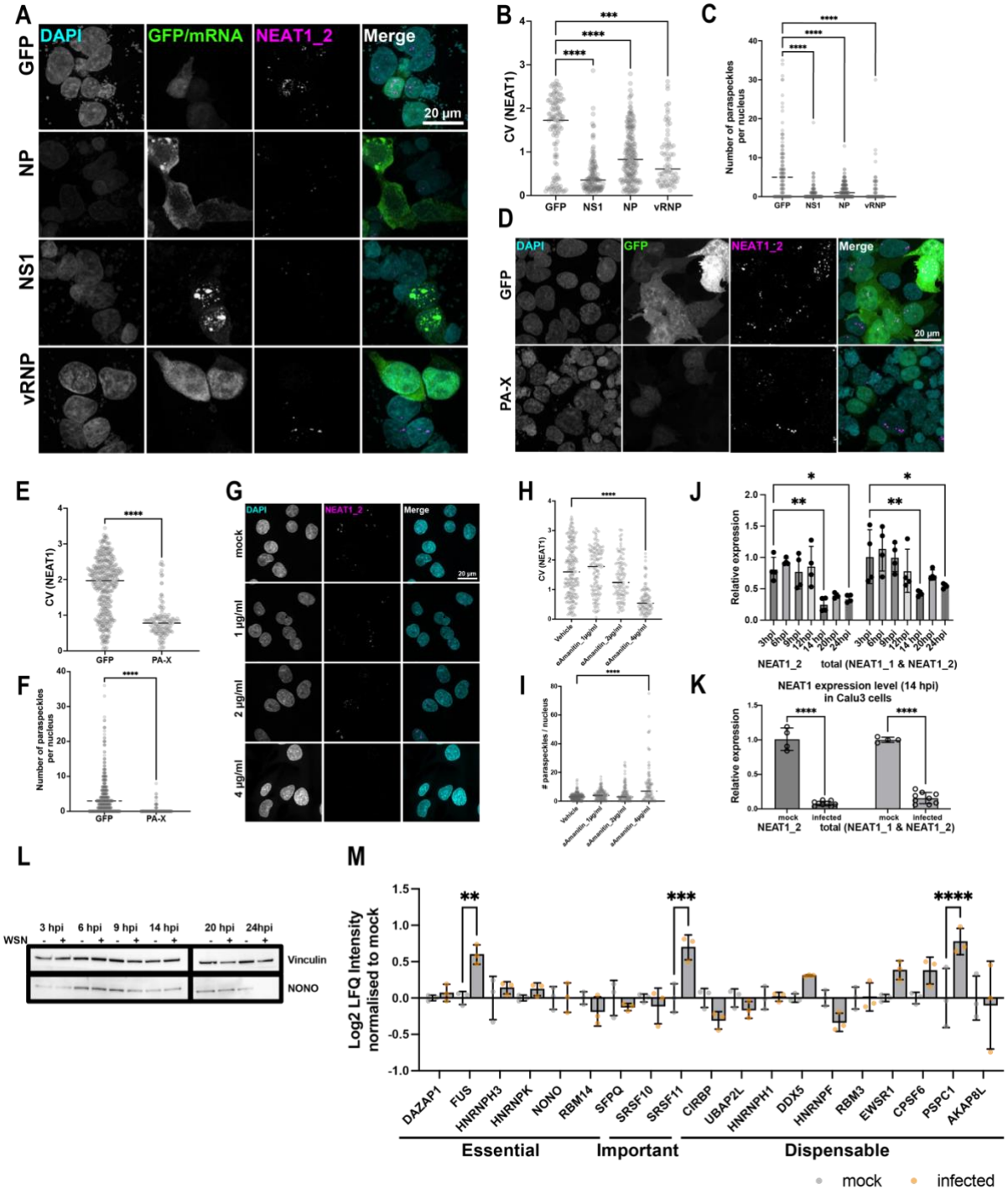

Figure 6. Mechanisms of paraspeckle disruption by IAV proteins

(A) Maximum projection of FISH confocal microscopy images of HEK293T cells transfected with either GFP (control), WSN viral proteins – NP, NS1, or a mini replicon vRNP system (including PA, PB1, PB2, NP and vRNA of NP), taken at 24 hpi. NEAT1_2 (paraspeckles) is shown in magenta, and GFP (control) or viral mRNAs (NP

or NS1) are indicated in green, DNA is counterstained with DAPI (cyan). Scale bar: 20 µm.

(B, C) CV of NEAT1_2 (B) and the number of paraspeckles per nucleus (C) across different conditions. Only GFP-positive cells were considered.

(D) Maximum projection of confocal microscopy images of HEK293T cells transfected with either GFP (control) or co-transfected with PA-X and GFP, taken at 24 hpt. NEAT1_2 (paraspeckles) is shown in magenta, and GFP is indicated in green, DNA is counterstained with DAPI (grey). NEAT1_2 is used as a marker for paraspeckles to assess the impact of IAV proteins on paraspeckle integrity.

(E,F) CV of NEAT1_2 in the nucleus and the number of paraspeckles per nucleus (F) across different conditions. Only GFP-positive cells were considered.

(G) Confocal images showing the maximum projection of NEAT1_2 (magenta) in A549 cells treated with different concentrations of α-Amanitin for 20 h. DAPI (cyan) counterstains the nuclei. Scale bar = 20 µm.

(H, I) CV of NEAT1_2 signal intensity (H) and the number of paraspeckles (I) per nucleus in A549 cells treated with α-Amanitin for 20 h.

(J) Quantitative PCR analysis of NEAT1_2 and NEAT1_1 expression in A549 cells infected with WSN (MOI 3) normalised to GAPDH and to the mock-infected condition at each corresponding time point (n=3).

(K) Quantitative PCR analysis of NEAT1_2 and NEAT1_1 expression in Calu-3 cells infected with WSN (MOI 3) normalised to GAPDH and to the mock-infected cells (n=3).

(L) Western blot analysis of NONO protein levels in A549 cells infected with WSN (MOI 3) at different time points post-infection (3, 6, 9, 14, 20, and 24 hpi). Vinculin serves as the loading control.

(M) Log_2 Label-Free Quantification (LFQ) intensity of paraspeckle proteins in A549 cells at 14 hpi with WSN (MOI=3), normalised to mock-infected cells.

(B-E, G-J, M) Data are represented as mean + SD. Statistical analysis was performed using ordinary one-way ANOVA. Statistical significance: *$p<0.05$, **$p<0.01$, ***$p<0.001$, ****$p<0.0001$.

Disruption of paraspeckles enhances IAV replication by liberating pro-viral host factors

To evaluate the functional relevance of paraspeckle disruption during infection, we used RNA interference to downregulate paraspeckle proteins and measured IAV replication by luciferase assay (Figure 7A). In agreement with our initial siRNA screen (Figure 2B), SFPQ knock-down decreased IAV replication in A549 cells, confirming its role in enhancing viral IAV RNA processing[85,86], whereas NONO knock-down had the opposite effect. In addition, we observed pro-viral effects when knocking down FUS and NEAT1 (Figure 7A). NEAT1 and NONO knockdown substantially upregulated vRNA, cRNA, and mRNA levels of NP and HA, as shown by strand-specific qPCR[97] (Figure 7B, Figure S8A-C). In contrast, SFPQ knockdown downregulated all these viral RNAs, aligning with its role in IAV RNA processing[85,86]. Knockout of NEAT1 and NONO impaired paraspeckle formation and increased IAV replication by 2–2.5-fold (Figure S8F-G, Figure 7C-D, Figure S8I-K) . Overexpressing mEGFP-NONO in wild-type cells impaired IAV replication by 30%, supporting an antiviral role of NONO (Figure 7E). Supplementing mEGFP-NONO in NONO KO cells reduced viral replication (significantly in one clone and without reaching statistical significance in the second clone, Figure 7E). Similarly, a minimal NEAT1_2[98] construct partially rescued paraspeckle formation, whereby a low expression level of NEAT_2 (5 %) likely prevented a more complete rescue (Figure S8H).

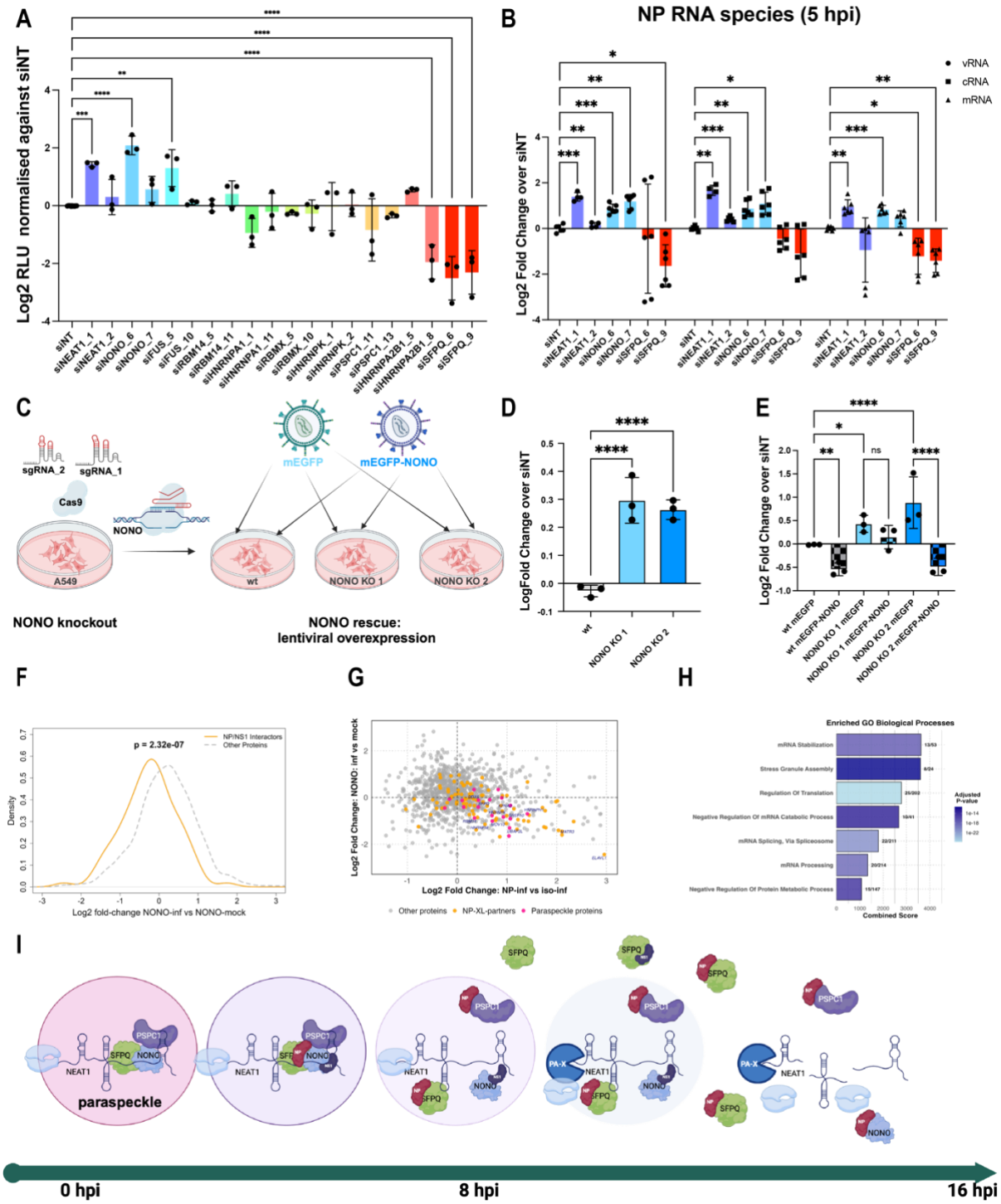

Figure 7. Functional analysis of paraspeckles during IAV infection.

(A) Luciferase activity in A549 cells transfected with siRNAs targeting paraspeckle components. Data are represented as mean ± SD (n = 3). siNEAT1_1 and 2 indicate two different siRNAs both targeting the whole NEAT1.The data for RBM14, RBMX, RBM5, HNRNPA1, HNRNPA2B1, HNRNPK and PSPC1 were reproduced from Figure S4C.

(B) Quantitative PCR analysis of viral RNA species of fragment NP normalised to GAPDH in A549 cells with knockdowns of paraspeckle proteins, infected with WSN (MOI 3) at 6hpi. Data are presented as log-fold-change of as mean ± SD relative to the siNT condition (n=3).

(C) Schematic of NONO knockout and rescue workflow. CRISPR-Cas9 with two sgRNAs generated NONO KO1 and KO2 A549 cell lines. Lentiviral overexpression of mEGFP-NONO or mEGFP (control) in KO cells was used for rescue. Wild-type, NONO KO, and rescued cells were analysed for paraspeckle function and viral replication. Created in BioRender. https://BioRender.com/t41h404

(D) Luciferase activity in wt, NONO KO1, and KO2 in A549 cells (WSN with PB2-T2A-NanoLuc, MOI 0.01, 48 hpi). Data are represented as mean ± SD (n = 3).

(E) Luciferase activity in wt, NONO KO1, and KO2 A549 cells lentivirally overexpressing mEGFP (control) or mEGFP-NONO (WSN with PB2-T2A-NanoLuc, MOI 0.01, 48 hpi). Data are represented as mean ± SD (n = 3).

(F) Density plot of log2-fold-changes of proteins cross-linked to NONO, NP and NS1 identified by AP-MS (NONO infected vs. NONO mock). Proteins cross-linked to NP and NS1 (orange) are co-depleted in infected cells compared to proteins not linked to NP or NS1 (grey).

(G) Log2-fold changes of interactors identified by AP-MS against NONO (infected vs. mock) and NP (infected vs. infected isotype control). Proteins cross-linked to NONO (pink), NP (orange), and non-associated proteins (grey) are shown.

(H) Selected protein categories enriched in both NP and NONO-mock AP-MS datasets from G (see also Table S3).

(I) Schematic representation of paraspeckles disruption: IAV proteins, particularly NP and NS1, disrupt paraspeckle integrity by binding core proteins like SFPQ and NONO, and possibly NEAT1, initiating paraspeckle disassembly. As the infection progresses, PA-X promotes NEAT1 degradation, while POL II inhibition further destabilises paraspeckles, leading to their complete disruption. Created in BioRender. https://BioRender.com/y54j344

(A-B, D-E) Data are represented as mean ± SD. Statistical analysis was performed using ordinary one-way ANOVA. Statistical significance: *p<0.05, **p<0.01, ***p<0.001, ****p<0.0001.

To test whether proteins that play roles during IAV infection but are normally sequestered within paraspeckles become available for interaction with IAV proteins upon infection (Figure S8B-C), we compared protein levels in AP-MS targeting NONO in infected cells (disrupted paraspeckles) with non-infected cells (intact paraspeckles). Indeed, proteins cross-linked with NP or NS1 were depleted from the NONO interactome in infected cells (Figure 7F, Figure S8L-M). Importantly, these changes were not due to infection-induced changes in overall protein levels, as input samples showed no differences between infected and mock-infected cells (Figure S8O-Q). This suggests that IAV infection triggers a redistribution of interactors from NONO to viral proteins. In support of this, the key RNA-binding proteins (RBPs) HNRNPC, HNRNPA1, MATR3, SFPQ, and HNRNPK are enriched in AP-MS targeting NP but depleted in AP-MS targeting NONO in infected cells (Figure 7G-H). Considering that all these RBPs are known regulators of paraspeckle integrity, RNA processing and transcriptional control[82,99–101], their liberation from NONO and engagement with NP/NS1 may conceivably enhance viral replication. Such a mechanism would be in line with the proviral effects of SFPQ we observed, as well as the documented roles of SFPQ and HNRNPK in IAV RNA splicing and replication[7,8,85,86,102].

Discussion

Our in-cell XL-MS using SHVIP provides a high-resolution spatial map of PPIs in IAV-infected cells, revealing host-pathogen contact sites within their native cellular environment. Unlike prior IAV interactome studies based on AP-MS or Y2H, which rely on lysed cells and disrupt native complexes, our approach preserves physiological interactions and captures contacts specific to a late infection stage. For example, the dataset lacks known PPIs from earlier infection stages, e.g. between RNA polymerase II and RdRp[103,104] as well as between the LRR domains of IAV replication co-factor ANP32 and the RdRp subunit PB2[35,105,106]. Instead, the ANP32A/B LRR domains cross-linked with the C-terminal region of M1. This suggests that, at a late infection stage, M1 may obstruct the ANP32A/B-RdRp interface, potentially inactivating replication and transcription, and thus freeing vRNPs for export from the nucleus.

Furthermore, our data enabled us to trace the steps of HA maturation and export through the secretory pathway (Figure 4C). Beyond implications for understanding the IAV infection cycle, these findings highlight the utility of in-cell XL-MS for reconstructing sequential steps of molecular pathways involved in infection.

Guided by SHVIP, we discovered that IAV actively disrupts paraspeckles, membraneless organelles involved in stress responses, immune regulation, and nuclear protein sequestration[74,77,79]. We propose that paraspeckle disassembly benefits IAV in two ways. First, it liberates host RNA-binding proteins essential for viral replication. This includes SFPQ, known for its role in IAV RNA expression[86], as well as HNRNPC and HNRNPA1, which likely facilitate viral RNA synthesis and nuclear transport[88,107,108]. Second, paraspeckle disassembly may suppress antiviral responses. Given their roles in stress adaptation and immune signalling, and our findings that NEAT1 and NONO restrict viral replication/transcription, the loss of paraspeckles could attenuate host antiviral gene regulation[109,110]. Thus, we posit that paraspeckle dismantling is an active viral strategy rather than a secondary consequence of host transcriptional repression.

Interestingly, while paraspeckles disappeared in IAV-infected A549 and Calu-3 cells, they persisted in HeLa cells infected with IAV, according to a previous study[85]. HeLa cells are less permissive to IAV[111–115], and this may reflect an inability of the virus to counteract paraspeckle-mediated antiviral functions in restricted infections. Moreover, our data on NEAT1_2 depletion align with evidence showing increased non-canonical splicing of the long isoform (NEAT1_2) during IAV infection, possibly due to NEAT1_2 release from paraspeckles, increasing its availability for splicing[116]. Notably, other viruses, such as Hantavirus[117], HSV-1[85,118], and Dengue virus[119], induce NEAT1 expression and enhance paraspeckle formation rather than disrupting them. However, for IAV, the diffused paraspeckle staining and weaker NEAT1_2 upregulation compared to HSV-1 were noted[116]. This may reflect a fundamental difference in viral countermeasures: IAV actively dismantles paraspeckles to hijack their protein components, while other viruses may tolerate or exploit them for antiviral signalling.

While validating all PPIs and contact sites in our map is beyond the scope of a single study, our snapshot provides a foundation for numerous follow-up investigations. For instance, we found five viral proteins, including all three polymerase subunits, cross-linked with calcium homeostasis-related proteins. Individual knockdowns did not

significantly affect infection (Figure S4), likely due to functional redundancy. However, these interactions align with previous reports linking calcium levels to influenza virus infection[4,58,120], supporting a novel hypothesis that calcium-mediated effects on infection involve viral interactions with calcium-binding proteins.

In the future, in-cell XL-MS of IAV-host interactions could be extended to other IAV strains and to earlier infection stages to capture the dynamics of these interactions, including those involving IAV RdRp during transcription[103,105]. Although AlphaFold has limitations in modelling host-pathogen interactions, and only a subset of PPIs could be modelled here, future advancements in structural prediction—particularly those integrating cross-links as restraints—could use XL-MS data to provide a detailed map of the structural interface between IAV and human proteins.

In conclusion, our work provides a vast and unique resource of native IAV-host PPIs and serves as a blueprint demonstrating how integrating in-cell XL-MS, functional analyses, and structural modelling can reveal the native structural interface between IAV and host proteins and uncover mechanisms of viral subversion.

Methods

Cell culture

The human lung epithelial cell line A549 (86012804) and the human HEK293T (120220101) cell line were purchased from European Collection of Authenticated Cell Cultures (ECACC) and were grown under standard conditions (37 °C and 5% CO2) in Dulbecco's modified Eagle's medium (DMEM) (Gibco, 11960044) supplemented with 10% fetal bovine serum (FBS) (Gibco, 0270106), GlutaMAX (Gibco 35050038), Sodium pyruvate (Gibco 11360039), penicillin–streptomycin (Gibco™ 15070063). Human Calu-3 cells (kind gift from Petr Chlanda) were cultured in DMEM and supplemented with 20% FBS, penicillin–streptomycin, GlutaMax and sodium pyruvate.

MDCK (ECACC, 84121903), MDCK.II (ECACC, 00062107) and MDBK (kind gift from Ervin Fodor) cells were cultured in Minimum Essential Media (MEM) supplemented with 10% FBS, penicillin–streptomycin, glutaMax and sodium pyruvate.

Mouse embryonic fibroblasts (MEFs) (kind gift from G. Gabriel) were cultured in DMEM Minimum Essential Media supplemented with 10% FBS, penicillin–streptomycin, glutaMax, sodium pyruvate and non-essential amino acids solution.

Human Bronchial Epithelial Cells (HBEpC) (Promocell C-12640, lot#499Z012.1) were cultured in ready-to-use Airway Epithelial Cell growth media (Promocell C-21060).

All cell lines were routinely tested for the absence of mycoplasma contamination using MYCOPLASMACHECK from Eurofins.

Virus production

WSN (A/WSN/33) virus was produced in Madin-Darby CBovine Kidney (MDBK) cells. Briefly, confluent MDBK cells in a T75 flask were infected with an MOI of 0.001 in DMEM containing 0.5 % FBS. The infection was allowed to proceed for 36 hours at 37°C with 5% CO_2 until full cytopathic effects (CPE) were observed. After incubation, the supernatant containing the virus was harvested, clarified by centrifugation at 1,500 g for 10 minutes at 4°C to remove cell debris, and aliquoted for storage at -80°C.

pdm09 (A/California/04/2009) and H3N2 (A/Aichi/2/1968) viruses were produced in MDCK cells. MDCK cells were infected at a MOI of 0.001 in serum-free DMEM supplemented with 0.2 % BSA and 1 µg/mL TPCK-treated trypsin. The infections were carried out at 37°C with 5% CO_2 for 36-48 hours until full CPE were observed.

Supernatants were collected, clarified by centrifugation at 1,500 g for 10 minutes at 4°C, in case of successful HA-Assay virus was aliquoted for storage at -80°C.

Generation of Recombinant IAV Overexpressing NanoLuc on PB2

Recombinant influenza A virus expressing NanoLuc fused to the PB2 protein was generated using a 12-plasmid reverse genetics system[52]. The system included eight plasmids encoding the viral RNA (vRNA) segments and four plasmids expressing the supporting polymerase complex proteins (PB2, PB1, PA, and NP) under the control of a human RNA polymerase I promoter. The NanoLuc reporter gene was inserted in-frame at the N-terminus of the PB2 coding sequence, separated by a self-cleaving T2A peptide, allowing independent translation of NanoLuc and PB2.

HEK293T cells and MDCK cells were co-cultured in Opti-MEM supplemented with 0.2% BSA and 1 µg/mL TPCK-treated trypsin. Cells were transfected with the 12-plasmid system using Lipofectamine 3000 (Thermo Fisher Scientific) according to the manufacturer's instructions. Specifically, 0.5 µg of each vRNA-encoding plasmid and 0.25 µg of each protein expression plasmid were transfected into HEK293T cells. Six hours post-transfection, the medium was replaced with infection media (DMEM supplemented with 0.2% BSA, 100 U/mL penicillin, 100 µg/mL streptomycin, and 1 µg/mL TPCK-treated trypsin), and the co-cultured cells were incubated at 37°C with 5% CO_2.

Seventy-two hours post-transfection, the supernatant was collected, clarified by centrifugation at 300 × g for 5 minutes, and used to infect MDCK cells to amplify the virus. Successful virus rescue was confirmed by NanoLuc activity assay and immunostaining of PB2. Viral titres were determined by plaque assay using standard protocols.

HA assay

The HA assay was performed in 96-well round-bottom plates. Serial two-fold dilutions of the virus samples were made in PBS, with a starting volume of 50 µL per well. 50 µL of the prepared 0.5% chicken erythrocyte suspension was added to each well. The plate was gently mixed and incubated at 4°C for 30 minutes, followed by an additional incubation at room temperature for 30 minutes to allow hemagglutination to occur. The HA titre was determined by visually inspecting the wells for hemagglutination. The HA titre is defined as the highest dilution of the virus that causes complete agglutination

of erythrocytes, resulting in a uniform lattice across the well. The results were recorded in hemagglutination units (HAU).

Plaque Assay

For WSN, MDCK cells were seeded in 6-well plates and allowed to reach full confluence. Serial dilutions of WSN viral stock were prepared in infection media (DMEM with 0.2% BSA). 330 µL of each dilution was added to the wells, and plates were incubated at 4°C for 30 minutes followed by 30 minutes at 37°C with gentle rocking every 15 minutes. After the incubation, the cells were overlaid with media containing avicel, 0.2% BSA and 1x DMEM. After 72 hours, the overlay was removed, and the cells were washed with PBS and stained with 1% crystal violet for 5 minutes. Plaques were counted, and the viral titre was calculated in PFU/mL.

For pdm09 and H3N2, MDCK-II cells were seeded in 6-well plates, and serial dilutions of viral stocks were prepared in infection media (DMEM with 0.2% BSA). 330 µL of each dilution was added to the wells, and plates were incubated for 30 minutes at 4°C followed by 30 minutes at 37°C. After the inoculation period, cells were overlaid with media containing avicel, 0.2% BSA, 1 µg/mL TPCK-treated trypsin, and 1x DMEM, and incubated for 72 hours.

Following incubation, cells were fixed with 4% paraformaldehyde for 30 minutes at 4°C. Fixed cells were blocked with 0.3 % hydrogen peroxide (H_2O_2) for 15 minutes and incubated with anti-NP antibody (ThermoFisher MA5-42364 for Aichi and Abcam ab43821 for pdm09, dilution 1:1000) for 1 hour at room temperature. After washing, the cells were incubated with HRP-conjugated secondary antibody for 1 hour. Staining was performed using KPL TrueBlue substrate (Seracare) for 15 minutes to visualise the plaques. Viral titres were calculated in PFU/mL based on plaque counts.

$$Titre\left(\frac{PFU}{ml}\right) = \frac{(Number\ of Plaques\ \times\ Dilution factor)}{Volume\ of\ virus\ innoculum\ (mL)}$$

Luciferase assay

A549 cells were seeded at 0.1 × 10^6 cells per well in 24-well plates. 12 h later, cells were transfected in duplicates with 10 µM siRNAs using RNAiMAX (Thermo Fisher

Scientific) following the manufacturer's protocol. After 72 hours of incubation at 37°C with 5% CO2, the medium was aspirated, and cells were washed with infection media.

Cells were then infected with recombinant IAV WSN PB2-T2A-NanoLuc at an MOI of 0.01. After 48 hpi the medium was carefully removed, and cells were lysed with 200 µL of 1× Passive Lysis Buffer (Promega) per well. Lysates were incubated at room temperature for 20-30 minutes on a rocking platform.

For the luciferase assay, 25 µL of cell lysate was mixed with 25 µL of NanoGlo substrate (Promega) in a white opaque 96-well plate. After a 5–10-minute equilibration at room temperature, luciferase activity was measured using a luminometer with an integration time of 1000 ms.

qPCR

Total RNA was extracted from infected and mock cells using and reverse-transcribed into cDNA using the High-Capacity cDNA Reverse Transcription Kit (Thermo Fisher Scientific) according to the manufacturer's instructions. Quantitative PCR was performed with PowerUp SYBR Green Master Mix (Thermo Fisher Scientific) on a [specific qPCR machine] using gene-specific primers. The qPCR cycling conditions were 50°C for 2 minutes, 95°C for 2 minutes, followed by 40 cycles of 95°C for 15 seconds and 60°C for 1 minute. Melt curve analysis confirmed product specificity. Relative gene expression was calculated using the ΔΔCt method with [housekeeping gene] as the internal control. All reactions were conducted in triplicate.

FISH

Cells were seeded at a density of 10^5 cells/well in 24-well plates containing sterilised glass coverslips and grown overnight to reach 70–80% confluence. Cells were washed twice with 300 µL of DPBS and then fixed with 300 µL of 4% paraformaldehyde (PFA) in DPBS for 10 minutes at room temperature. Following fixation, cells were washed twice with 300 µL of DPBS, followed by overnight incubation with 300 µL of ice-cold 70% ethanol for permeabilization and stored at -20°C overnight or until further processing. The hybridization protocol was adapted from the method described by Choi et al. with optimisations for detecting vRNA, mRNA and cRNA from IAV. Fixed and permeabilised cells were air-dried briefly, followed by two washes with 2× SSC buffer. Cells were pre-hybridised with 300 µL of 30% Probe Hybridization Buffer (Molecular Instruments) at 37°C for 30 minutes. Probes specific to RNA of interest

were designed as described in the supplementary protocol and purchased from SigmaAldrich. A total of 2 pmol of each probe was added to 300 µL of 30% Probe Hybridization Buffer and applied to the cells. Hybridisation was carried out overnight at 37°C. After hybridisation, excess probes were removed by washing the cells four times with 300 µL of 30% Probe Wash Buffer at 37°C. Cells were subsequently washed twice with 5× SSCT at room temperature. Pre-amplification was performed by incubating the cells with 300 µL of Amplification Buffer (Molecular Instruments) at room temperature for 30 minutes. HCR hairpins (h1 and h2) were heated at 95°C for 90 seconds, followed by cooling to room temperature in the dark for 30 minutes. Snap-cooled hairpins were added to 300 µL of Amplification Buffer and applied to the cells. Amplification was allowed to proceed overnight at room temperature in the dark. Following amplification, excess hairpins were removed by washing the cells five times with 300 µL of 5× SSCT at room temperature. Cells were then stained with DAPI (1:30000 dilution in water) for 10 minutes at room temperature in the dark, followed by three washes with 1× PBS. For imaging, coverslips were mounted on glass slides using Dako antifade mountant (Agilent Technologies). Slides were sealed and stored at 4°C, protected from light, until imaging. Fluorescent signals were visualized using a confocal microscope equipped with appropriate filters for DAPI and the fluorescent labels used in the HCR hairpins. Imaging parameters were adjusted to minimize background and optimize signal detection.

siRNA transfection

All siRNAs were purchased from Qiagen (Table XXX). Transfections of siRNAs (5 pmol) were performed in A549 cells at 60% confluency using Lipofectamine RNAiMAX Transfection Reagent (Thermo Scientific, catalogue no. 13778075) according to the manufacturer's instructions. Efficiency of siRNA-mediated depletion was performed 72 h after transfection by either qPCR or western blotting.

Cell viability

Cell viability assays were conducted using the CellTiter-Glo® 2.0 Assay Kit (Promega, catalogue no. G9241). Cells were seeded in 24-well plates and treated as per experimental conditions. Following treatment, CellTiter-Glo® 2.0 Reagent was added directly to the culture medium, and plates were incubated at room temperature with gentle shaking for 10 minutes to induce cell lysis. Luminescence was then measured

using a plate reader to quantify ATP levels, which served as an indicator of cell viability. The obtained luminescence values were normalised to the control group to determine relative cell viability.

CRISPR/Cas 9-mediated knock-out cell lines

sgRNAs were designed using Benchling or ordered directly from IDT as verified sgRNAs. These were resuspended in nuclease-free water to a working concentration of 1 µM. Purified Cas9 protein was obtained from the EMBL HD Protein Production Facility and diluted in OptiMEM to 1 µM for use. A549 cells were seeded at 150,000 cells per well in 6-well plates, maintaining low cell density (<50% confluency) to ensure high knockout efficiency (>90%). Cells were incubated overnight at 37°C with 5% CO2.

RNP complexes were formed by combining Cas9 and sgRNA in OptiMEM and incubating briefly at room temperature. The RNPs were then mixed with Lipofectamine RNAiMAX and further incubated before being added to the cells. Transfected cells were incubated for 96 hours at 37°C with 5% CO2. Following transfection, cells from one well were harvested for genomic DNA (gDNA) extraction, while cells from the second well were seeded at 0.5 cells per well in 96-well plates for clonal selection. gDNA was extracted according to kit instructions (NEB), and PCR was performed to amplify the region flanking the sgRNA target site. The PCR products were resolved on an agarose gel, purified, and sequenced via Sanger sequencing. Knockout efficiency was evaluated using TIDE analysis [121], and Western blotting was conducted to confirm the absence of the target protein.

Plasmid transfection

Plasmid transfections were performed using Lipofectamine 3000 (Thermo Fisher Scientific) according to the manufacturer's protocol. HEK 293T cells were transfected at 70–80% confluency. On the day of transfection, the plasmid DNA was diluted in Opti-MEM I Reduced Serum Medium (Thermo Fisher Scientific). Separately, Lipofectamine 3000 reagent was also diluted in Opti-MEM. The diluted DNA and Lipofectamine 3000 were combined and incubated

at room temperature for 15 minutes to allow the formation of DNA-lipid complexes.

The DNA-lipid complexes were then added dropwise to the cells. The cells were incubated with the transfection mixture for 4–6 hours at 37°C in a humidified incubator

with 5% CO2. After incubation, the transfection medium was replaced with fresh complete growth medium, and cells were incubated for an additional 16–48 hours before downstream analyses.

Transfection efficiency was monitored by co-transfecting a GFP-expressing plasmid or by IF or FISH staining of proteins of interest, and the expression was assessed by fluorescence microscopy.

Lentiviral cell line generation

Lentivirus production was conducted in HEK293T cells by transfecting the lentiviral vector containing the genes of interest (NONO, PSPC1, and SFPQ tagged with mEGFP) along with packaging plasmids using a calcium phosphate transfection method. After 48 hours, lentivirus-containing supernatants were collected, filtered, and stored at -80°C until further use.

A549 cells were seeded in culture plates and infected with lentivirus-containing supernatants supplemented with polybrene for enhanced transduction efficiency. Following infection, cells were incubated for 48-72 hours to allow for stable integration of lentiviral constructs into the host genome.

To confirm successful lentiviral transduction and expression of the tagged proteins, fluorescence microscopy and western blotting were performed using appropriate antibodies and detection reagents. Expression levels of the tagged proteins were quantified using fluorescence intensity measurements or densitometry analysis of western blot bands.

The functionality of the tagged proteins was assessed using their ability to co-localise with NEAT1 to the paraspeckles. The lentivirus-infected cell lines expressing the tagged proteins were maintained in complete DMEM media supplemented with 10 µg/ml Blasticidin for positive selection.

RNA Extraction

RNA extraction was performed using the RNeasy kit from Qiagen according to the manufacturer's protocol. Briefly, cells were washed with PBS, lysed, and homogenized in buffer RTL supplemented with 5 mM TCEP. Following ethanol addition, the lysate was applied to an RNeasy column and washed successively with buffers RW1 and

RPE. Finally, RNA was eluted in RNase-free water, quantified using a NanoDrop spectrophotometer, and stored at -70°C until further use.

Reverse Transcription and qPCR

Total RNA (up to 2 µg per 10-µL reaction) was reverse transcribed using the High-Capacity cDNA Reverse Transcription Kit (ThermoFisher 4368814). Kit components were thawed on ice, and the RT master mix was prepared accordingly. RNA samples were diluted in RNase- and DNase-free water, added to the master mix, and sealed in reaction plates or tubes. The reverse transcription was performed according to the manufacturer's instructions.

Quantitative PCR (qPCR) was performed using primers listed in Table XX and the PowerUp SYBR Green Master Mix (ThermoFisher, catalogue no. A25742). Each reaction mixture consisted of 5 µl of PowerUp SYBR Green Master Mix, forward and reverse primers, template cDNA, and nuclease-free water. Thermal cycling was conducted according to the manufacturer's instructions, and fluorescence signals were monitored in real-time using a qPCR instrument. Analysis of the qPCR data was performed using the instrument's software to determine the relative gene expression levels.

Immunoblotting

Protein cell extracts were resolved by SDS–PAGE in precast protein gels (SERVAGel™ TG PRiME™ 4 - 12 %, catalogue no. 43274.01) and transferred onto nitrocellulose membranes (Biorad catalogue no. 1704158 and 1704159.) Membranes were blocked with 2.5% BSA powder diluted in TBS-Tween 20 (0.01%) for 1 h at room temperature. Incubation with primary antibodies in blocking solution was applied overnight at 4C. The following primary antibodies were used for western blot analysis: NONO mouse monoclonal (1:1,000, Proteintech, clone 2A2B10, catalogue no. 66361-1-Ig); NONO rabbit polyclonal (1:1,000, Proteintech, catalogue no. 11058-1-AP); SFPQ mouse monoclonal (1:1,000, Proteintech, clone 1G4A5, catalogue no. 67129-1-Ig); SFPQ rabbit polyclonal (1:1,000, Proteintech, catalogue no. 15585-1-AP); PSPC1 rabbit polyclonal (1:1,000, Proteintech, catalogue no. 16714-1-AP); SLC7A5 rabbit polyclonal (1:1,000, Proteintech, catalogue no. 28670-1-AP); SLC7A5 mouse monoclonal (1:1,000, Proteintech, clone 2G5H3, catalogue no. 67951-1-Ig); SLC3A2 rabbit polyclonal (1:1,000, Proteintech, catalogue no 15193-1-AP); SLC3A2 mouse

monoclonal (1:1,000, Proteintech, clone 2B10F5, catalogue no. 66883-1-Ig); NP mouse monoclonal (1:1,000, Abcam, clone C43, catalogue no. ab128193); M2 mouse (1:1,000, ThermoFisher, clone 14C2, catalogue no. MA1-082); PB1, PB2, M1 (1 :1000, Abcam ab22396), NS1 (1:1,000, ThermoFisher, MA5-35909); Vinculin mouse (1:5000, Merck, catalogue no. V9131) ; Cyclophilin B rabbit monoclonal (1:5,000, CST, clone D1V5J, catalogue no. 43603).

Following incubation with primary antibodies, three washes with TBS-Tween 20 (0.01%) were performed. Membranes were incubated with secondary horseradish antimouse or antirabbit peroxidase-coupled antibodies IgG (1:5000) for 1 h at room temperature followed by three washes with TBS-Tween 20 (0.01%), before detection by ECL-based chemiluminescence (ThermoFisher catalogue no. A38555). Uncropped Western blot images are included in the Source files corresponding to the respective figure.

SHVIP sample preparation

Cells were infected at an MOI of 5 as described above. At 5 hpi, cells were washed twice with PBS, and L-HPG-labelling medium was added, consisting of 500 µM HPG (Click Chemistry Tools), methionine-free DMEM (Gibco), and 0.2% BSA (Merck). Cells were washed in PBS and harvested by scraping at 14 hpi. For cross-linked samples, disuccinimidyl sulfoxide (DSSO) was added to a concentration of with 5 mM in a 1:1 (v/v) PBS/cell suspension after which samples were incubated for 1 h at room temperature under constant shaking. The cross-linking reaction was quenched by adding Tris (pH 8.0) to a final concentration of 30 mM for 20 min. Cells were lysed in a buffer containing 200 mM Tris (pH 8.0), 4% 3-((3-cholamidopropyl) dimethylammonio)-1-propanesulfonate (CHAPS), 1 M NaCl, 8 M urea, and protease inhibitors and frozen at -80°C until HPG enrichment.

For enrichment of HPG-labelled proteins lysates were thawed, genomic DNA was removed by addition of Benzonase and lysates were sonicated using a Bioruptor Pico (Diagenode) with 10 cycles of alternating between 30 s sonication and 30 s pause. Lysates were centrifuged at 10,000 g for 10 min. 800 µl of each lysate was mixed with 200 µl picolyl-azide agarose (Click-&-Go® Plus Protein Enrichment Kit, Click Chemistry Tools, now part of Vector Laboratories) saving 50 µl of each lysate as input samples. Enrichment of of HPG-labelled proteins was performed as described before

[29]. In brief, after addition of cupper-(i)-catalyst solution, samples were rotated head-over-tail at room temperature overnight. Proteins were reduced by addition of 10 mM DTT and incubation at 70 °C for 15 min, followed by alkylation by addition of 40 mM Chloroacetamide (CAA) and incubation room temperature in the dark. Beads were subsequently washed in gravity flow columns (Pierce, Thermo Scientific) 10 times each with 1% w/v SDS, 250 mM NaCl, 5 mM EDTA in 100 mM Tris (pH 8.0); 8 M urea in 100 mM Tris (pH 8.0); 80% v/v acetonitrile (ACN) in water; 5% v/v ACN in 50 mM triethylammonium bicarbonate (TEAB); 2 M urea plus 5% v/v ACN in 50 mM TEAB. Afterwards, captured proteins were digested in the last washing buffer by addition of trypsin and lysyl-endopeptidase C (LysC) and overnight incubation at 37°C. Peptides were recovered by collecting the supernatant, followed by acidification with adding 1 % (v/v) formic acid (FA). Peptides were desalted using C18 stage tips[121] for bottom-up samples or using C8 1cc Sep-Pak columns (Waters) according to manufacturer's protocol and finally dried in speed-vacuum. Peptides were stored dry at -20°C until LC-MS measurement or subjected to further off-line fractionation.

Proteins from input samples were extracted by methanol/chlorophorm precipitation[122] and resuspended in digestion buffer consisting of 1% w/v SDC, 5 mM Tris-(2-carboxyethyl)phosphin (TCEP), 40 mM CAA in 50 mM TEAB (pH 8.0). Proteins were digested with trypsin and LysC and finally desalted as described above.

Off-line fractionation of cross-linked peptide samples

To further separate cross-linked peptides from linear peptides, samples were resuspended in 0.1 % (v/v) FA and subjected to strong cation exchange chromatography (SCX) using an Agilent 1260 Infinity II HPLC system and a PolySULFETHYL A column (PolyLC) column. Samples were fractionated by applying a linear 95 min gradient going from buffer A (20 % v/v ACN in milli-Q water) to a mixture of 20% buffer A and 80 % buffer B (5 M NaCl, 20 % v/v ACN in milli-Q water). Fractions were collected in 45 s intervals, desalted as described above, dried in speed-vacuum and stored at -20 °C until measurement. After measurement, enriched samples were pooled in groups of 2 to 4 SCX fractions and subjected to size exclusion chromatography (SEC) using a SuperdexTM 30 Increase 3.2/300 column (GE Healthcare) with a 60 min run with running buffer consisting of 30 % (v/v) ACN and 0.1 % (v/v) trifluoroacetic acid (TFA) in milli-Q water, collecting fractions in 2 min intervals. Samples were dried in speed-vacuum and stored at -20 °C until measurement.

Pulldown

HEK 293T cells were transfected with TwinStrep-NONO, TwinStrep-M2, or TwinStrep-tagged empty vector (control) using PEI at ratio 1:3. Each construct was overexpressed in separate 10 cm dishes, and 24 hours post-transfection, cells were harvested. Cells were detached by gentle scrapping in PBS, followed by washing with PBS. The cell pellets were lysed in 300 µl of IP lysis buffer (Thermo Fisher) supplemented with 1xHALT Protease inhibitor (Thermo Fisher). Lysates were clarified by centrifugation at 17,000 g for 20 min at 4°C.

Magnetic beads (5% suspension) were prepared by resuspending and equilibrating in 1x Buffer W (IBA Lifesciences) as follows: for each 250 µl lysate sample, 100 µl of the bead suspension (5 µl of beads) was added to a microcentrifuge tube. Beads were washed three times with 500 µl of 1x Buffer W on a magnetic separator to remove supernatant between washes.

After washing, beads were resuspended in 250 µl of lysate containing TwinStrep-tagged proteins and incubated for 1 h at room temperature rolling to keep the beads in suspension. Following incubation, beads were washed three times with 500 µl of 1x Buffer W (IBA Lifesciences). Bound proteins were eluted under denaturing conditions by adding 125 µl of Laemmli buffer and heating 95°C for 2 min. Eluates were analysed by Western blot or other.

Immunoprecipitation

A549 cells were seeded in 10 cm dishes at a density of 4 × 10^6 cells per dish and infected with WSN (MOI 3) for 14 hours. After infection, cells were harvested, and washed with PBS, scraped into 15 mL Falcon tubes, and centrifuged at 300 g for 5 minutes at 4°C. The cell pellets were washed once more with PBS and lysed in 600 µL IP lysis buffer (Thermo Fisher, #87786) supplemented with 1x HALT protease inhibitor (Thermo Fisher, #87786). For IP of NONO, SFPQ, PSPC1 and NP 0.1% SDS was added to reduce non-specific binding. Lysates were incubated on ice for 20 minutes and vortexed briefly. After incubation, the lysates were cleared by centrifugation at maximum speed for 20 minutes at 4°C. Supernatants were transferred to fresh tubes.

500 µL of cleared lysate was incubated with 10 µg of antibody [e.g., NP (ab128193), M2 (MA1-082), NS1 (ab91642), NONO (11058-1-AP), etc.] for 4 hours at 4°C with

gentle agitation. Isotype control antibodies (e.g., anti-rabbit IgG, Thermo Fisher #31887; anti-mouse IgG, Thermo Fisher #31878) were included in all experiments. For each IP, 25 µL of Pierce™ Protein A/G Magnetic Beads (Thermo Fisher, #88802) or Dynabeads™ Protein G (Thermo Fisher, #10003D) was equilibrated in 175 µL of Wash Buffer (TBS with 0.05% Tween-20), washed twice with Wash Buffer, and once with IP lysis buffer without detergents. The antibody-lysate mixture was added to the pre-washed beads and incubated for 1 hour at room temperature with constant mixing.

Beads were washed three times with 500 µL of Wash Buffer and two additional times with lysis buffer without detergents. A final wash was performed with TBS without Tween-20. For subsequent mass spectrometry analysis (affinity purification mass spectrometry, AP-MS), proteins were eluted by adding 100 µL of pre-warmed 8M GndHCl (Thermo Fisher, #24115) to the beads, incubating at 95°C for 2 minutes with shaking. Afterwards, proteins were precipitated by adding the eluate to 900 µl pre-cooled LiChrosolv ethanol and overnight incubation at 4°C. Precipitated proteins were collected by centrifugation at 18,000 g for 1 h, discarding the supernatant by decanting. Additionally, aliquots before immunoprecipitation (input) were taken and processed by methanol/chloroform precipitation, as descried above. For western blot analysis, elution was performed with 0.2 M Glycine (pH 2.0) for 10 minutes at room temperature, followed by neutralization with 1 M Tris (pH 8.0). A second elution was performed using 100 µL of SDS-PAGE reducing sample buffer, with samples heated at 96-100°C for 10 minutes.

Eluates were analysed by SDS-PAGE and Western blotting to detect the immunoprecipitated proteins using appropriate primary and secondary antibodies or analysed by mass spectrometry as described below including 20 µl of input per sample. All AP-MS experiments were conducted in triplicates.

LC-MS/MS of bottom-up proteomics and AP-MS samples

Bottom-up proteomics samples were measured on a Orbitrap Fusion Tribrid mass spectrometer (Thermo Fisher Scientific) operating with instrument control software version 3.4. Peptides were resuspended in 1 % (v/v) FA and 0.5 % (v/v) acetonitrile (ACN) in milli-Q water. Approximately 1 µg of peptides were loaded on an in-house packed 50 cm analytical, reverse-phase column (Poroshell 120 EC-C18, 2.7 µm, Agilent Technologies) using an online connected Ultimate 3000 RSLC nano LC

system (Thermo Fisher Scientific). Peptides were separated by 120 min or 180 min gradients starting from 0.1% v/v FA in water (buffer A) to 0.1% v/v FA in 80% v/v ACN (buffer B) at a flow rate of 250 nl/min.

Peptides were detected with an HCD-MS2 (higher-energy collisional dissociation) method with MS1 scans acquired in the Orbitrap at a resolution of 120,000 with intervals of master scans set to 1s. Scan range was set to 375-1500 (m/z), AGC target to “Standard” and maximum injection time set to 50 ms. Intensity threshold was set to 1E+04. Dynamic exclusion of precursors was set to 40 s. Precursors of charge state +2-+4 were selected for fragmentation with a precursor isolation window of 1.6 m/z and fragmented with a single HCD energy of 30%. MS2 scans were acquired in the ion trap with scan rate set to “Rapid” and AGC target of 100%.

AP-MS samples were measured on an Orbitrap Exploris 480 (Thermo Fisher Scientific) operating with instrument control software version 4.2 and online connected to a Vanquish neo UHPLC system (Thermo Fisher Scientific). Liquid chromatography was performed as described above for bottom-up samples. MS1 scans were performed in the Orbitrap with resolution set to 120,000 and cycle times set to 2 s enabling dynamic exclusion of 40 s. Intensity threshold was set to 1E+04, the maximum injection time to “Auto” and AGC target to 300%. Precursors of charge +2-+4 were isolated with a window of 1.6 m/z. Fragmentation was performed by HCD energy of 30 %. Fragments were detected in MS2 in the Orbitrap with a resolution set to 15,000 and AGC target set to “Standard”.

LC-MS/MS of cross-linked samples

Cross-linked peptides were detected with an Orbitrap Fusion Lumos Tribrid mass spectrometer (Thermo Fisher Scientific) run with instrument control software version 4.0 and equipped with a FAIMS Pro Duo interface (Thermo Fisher Scientific). Chromatographic separation of peptides was conducted as described above. FAIMS compensation voltages were alternated between -50, -60 and -75 V.

Cross-linked samples were measured with a stepped-HCD-MS2 method. MS1 scans were acquired in the Orbitrap with the resolution of 120,000. The following parameters were used: scan range 375-1600 m/z; “Standard” settings for AGC target; injection time 50 ms; precursor charge state +4-+8, isolation window 1.6 m/z, dynamic exclusion 60 s, cycle time 2 s and stepped-HCD energies of 21 %, 27 % and 33 %.

MS2 scans were acquired in the Orbitrap with a resolution of 60,000, mass range set to “Normal” and scan range set to “Auto”. Maximum injection time was set to 118 ms and AGC target to 200 %.

Bottom-up proteomics data analysis

Raw files were searched with MaxQuant version 1.6.2.6a[123] with standard parameters, the match between runs and second peptides enabled against the SwissProt human reference proteome (downloaded 2020, containing 20,365 target sequences), and IAV sequences of IAV/WSN/1933(H1N1) (containing 15 target sequences). Trypsin was set as a digestion enzyme. The minimum peptide length was set to 7 amino acids with a maximum of 2 missed cleavages and results were filtered to 1 % false discovery rate (FDR) on PSM and Protein level using reversed decoy sequences. Carbamidomethylation of cysteine was set as fixed modification, and oxidation of methionine, acetylation of protein N-termini as well, and replacement of methionines with homopropargylglycine (HPG) were set as variable modification when appropriate. Intensity-based absolute quantification (iBAQ) was enabled. ProteinGroups.txt table was used for further data analysis in R analysing contribution of viral and host proteins in input and enriched samples after the removal of contaminants, decoy hits and proteins only identified by a modification site.

AP-MS data analysis

Raw files for AP-MS experiments were searched with MaxQuant version 1.6.2.6a with parameters set as described above plus label-free quantification (LFQ) enabled with a minimum of 2 peptide ratios required for quantification. ProteinGroups.txt table was used for data analysis in R analysing LFQ values of proteins in all 3 technical replicates. Contaminants, decoy hits and proteins only identified by a modification site were removed and LFQ values were log2 transformed. Missing values were imputed as described before[124] on the basis of a normal distribution across of LFQ values shrunk by a factor of 0.3 and downshifted by 1.8 standard deviations when quantification values were available in all three replicates of experiment or control. Log2 fold changes between control and experiment were calculated as the average across the three respective replicates and significance was assessed by calculating p-values of two-sided t-test. For the analysis of input samples related to the AP-MS

experiments, we searched all raw-files with MaxQuant version 2.2. using the same parameter settings.

Cross-linking mass spectrometry data analysis

Raw files were searched using Scout[125] version 1.5.1 against a database containing sequences of all proteins found in the enriched bottom-up proteomics samples. Pre-settings for DSSO cross-linker were used (light fragment mass 54.01056468 Da, heavy fragment mass 85.98263585 Da, full mass 158.00376533 Da, mass shift 31.97207117 Da) with residue specificity for lysine, serine, threonine, and tyrosine. The minimum peptide length was set to 6 amino acids with a maximum of 3 missed cleavages, precursor mass tolerance was set to 10 ppm, and fragment mass tolerance to 20 ppm. Carbamidomethylation of cysteine was used as a static modification, and oxidation of methionine as a variable modification. Results were filtered to reach either a 2 % FDR or a 5 % FDR on cross-link spectrum match (CSM), peptide pair level and on protein-protein pair (PPI) level. For assessment of replicate-to-replicate reproducibility and performance (Figure S1M-R), only raw files from SCX fractionated samples were searched individually per replicate, imposing a 2 % FDR cut-off at CSM, residue-pair, and PPI-level. For creating the complete cross-linking data set, all replicates, as well as raw files from SCX and SEC fractionated samples, were searched together.

Confocal microscopy

All imaging was conducted using a Nikon Ti2 microscope equipped with a CSU-W1 spinning disk confocal unit and an Andor DU-888 X-11633 camera. The microscope was controlled by NIS-Elements software and utilized a 100x/1.49 SR Apo TIRF AC oil immersion objective (Nikon). For live-cell imaging, cells were seeded in Ibidi µ-Slide 4-well chambers (Ibidi USA, NC0685967) and maintained at 37°C with 5% CO_2. Imaging was performed using the 405 nm (DAPI channel), 488 nm (GFP channel), and 561 nm (Cy5 channel) lasers, with exposure times optimised for each experiment. The camera was maintained at -69.4°C, with a binning of 1x1 and a readout speed of 30 MHz. Z-stacks were captured with an interval size of 130.6 nm, and images were acquired at a resolution of 1024x1024 pixels.

Image Analysis

All images were processed as maximum intensity projections (MaxIP). Nuclei (DAPI) and paraspeckles (NEAT1_2) were segmented using CellProfiler with the Otsu thresholding method. The coefficient of variation (CV) of the NEAT1_2 signal within nuclei and the number of segmented paraspeckles were used as independent metrics. Both metrics have their respective advantages and disadvantages. While CV relies on more reliable nuclei segmentation, it is an indirect measure of paraspeckle integrity and does not provide precise structural information. In contrast, paraspeckle quantification directly assesses paraspeckle formation but is more error-prone, particularly at later time points when the NEAT1_2 signal diminishes.

Validation of cross-links by host structures and AlphaFold 2 models

For each cross-linked human protein, all structures for this protein were retrieved from the Protein Data Bank (PDB) based on the corresponding UniProt ID using both UniProt[126] website REST API and RCSB PDB Search API[127]. All cross-linked pairs were mapped to the retrieved structures, and if the corresponding pair was found among structures, C_α-C_α was calculated. If one pair was mapped to multiple structures, the shortest C_α-C_α distance was taken. The same mapping procedure was used for the random cross-linked pairs generated by taking arbitrary lysine-lysine pairs for individual proteins and protein pairs detected in PPIs. AlphaFold2[44] models were built using AlphaPulldown[128]. Structural figures were rendered using UCSF ChimeraX[129].

Virus-host interaction structural modelling

AlphaFold 2[44] models were built using AlphaPulldown[128] version 2.0 using 24 recycles. The sequence and template databases as of August 2024 were used. AlphaFold 3[46] was run using the original AlphaFold 3 code and using the default sequence database (downloaded in November 2024) and PDB database from November 2021 using the download script provided in AlphaFold 3. AF3x[47] was run with default settings and using version #dfb94a3 and the same databases as AlphaFold 3. The quality of models was assessed using interface predicted template modelling (ipTM) score, predicted template modelling (pTM), residue's predicted local distance difference test (pLDDT) score, and predicted alignment error (PAE), as returned by all the above tools. Structural figures were rendered using UCSF ChimeraX[129].

Other bioinformatics analyses

Functional enrichment analysis was performed using the Enrichr web platform[130]. The default Fisher's exact test with the Benjamini-Hochberg method for correction for multiple hypotheses testing was used. For cross-links to viral proteins where alternative proteins with identical cross-linked peptide sequences were detected ambiguously (e.g., histone proteins), only the first protein from the list of ambiguous candidates was selected for the analysis. Cross-link diagrams were drawn using xiNET[131].

Data availability

Mass spectrometry data will be deposited in the PRIDE database. Structural models will be made available on Zenodo upon publication. Fluorescent images will be deposited in the BioImage Archive.

Code availability

Not applicable.

Acknowledgements

DY and JK have been supported by the German Research Foundation (DFG) grant ID: KO 5979/2. KG and JK were supported by DFG VISION grant ID: GRK 2887/1. JK was supported by ERC (TransFORM, 101119142). F.L and L.M have been supported by DFG Project LI 3260/6-1 and F.L was supported the Leibniz-Wettbewerb (P70/2018). B.B. acknowledges funding from Deutsche Forschungsgemeinschaft (https://www.dfg.de/en/index.jsp) grant BO 5917/1-1. This project received funding from the FEBS Excellence Award, of the Deutsche Forschungsgemeinschaft (DFG project number 506356718/ DU 2279/2-1) and the European Molecular Biology Laboratory to O.D. We thank Dr. Ying Wang for her support in the lab, Valentin Mauer for assistance with statistical analysis, and Dr. Lucas DeFelipe for guidance on figure preparation and adherence to publication standards. We thank Caroline Demeret and Nadia Naffakh for critical reading and helpful comments on the manuscript.

Author contributions

I.K., F.L., B.B., and J.K. conceived and designed the study. I.K., L.M., and B.B. performed experiments, K.G. performed structural analyses and modelling, and created diagram figures, D.Y. contributed to structural modelling, D.Z. helped with data analysis, K.B performed experiments, O.D. supervised experiments, S.S.B and S.B performed experiments, G.B. supervised experiments. I.K., L.M., B.B., K.G, and J.K. analysed data. I.K., B.B., K.G., and J.K. wrote the manuscript. All authors revised the manuscript.

Declaration of interests

The authors declare no competing interests.

Declaration of generative AI and AI-assisted technologies

During the preparation of this work, the authors used ChatGPT and Grammarly to improve the style and grammar of the text. After using this tool or service, the authors reviewed and edited the content as needed and take full responsibility for the content of the publication.

References

1. Krammer, F., Smith, G.J.D., Fouchier, R.A.M., Peiris, M., Kedzierska, K., Doherty, P.C., Palese, P., Shaw, M.L., Treanor, J., Webster, R.G., et al. (2018). Influenza. Nat. Rev. Dis. Primer *4*, 1–21. https://doi.org/10.1038/s41572-018-0002-y.

2. Eisfeld, A.J., Neumann, G., and Kawaoka, Y. (2015). At the centre: influenza A virus ribonucleoproteins. Nat. Rev. Microbiol. *13*, 28–41. https://doi.org/10.1038/nrmicro3367.

3. Karlas, A., Machuy, N., Shin, Y., Pleissner, K.-P., Artarini, A., Heuer, D., Becker, D., Khalil, H., Ogilvie, L.A., Hess, S., et al. (2010). Genome-wide RNAi screen identifies human host factors crucial for influenza virus replication. Nature *463*, 818–822. https://doi.org/10.1038/nature08760.

4. König, R., Stertz, S., Zhou, Y., Inoue, A., Hoffmann, H.-H., Bhattacharyya, S., Alamares, J.G., Tscherne, D.M., Ortigoza, M.B., Liang, Y., et al. (2010). Human host factors required for influenza virus replication. Nature *463*, 813–817. https://doi.org/10.1038/nature08699.

5. Bortz, E., Westera, L., Maamary, J., Steel, J., Albrecht, R.A., Manicassamy, B., Chase, G., Martínez-Sobrido, L., Schwemmle, M., and García-Sastre, A. (2011). Host- and strain-specific regulation of influenza virus polymerase activity by interacting cellular proteins. mBio *2*, e00151-11. https://doi.org/10.1128/mBio.00151-11.

6. Naito, T., Momose, F., Kawaguchi, A., and Nagata, K. (2007). Involvement of Hsp90 in Assembly and Nuclear Import of Influenza Virus RNA Polymerase Subunits. J. Virol. *81*, 1339–1349. https://doi.org/10.1128/jvi.01917-06.

7. Thompson, M.G., Muñoz-Moreno, R., Bhat, P., Roytenberg, R., Lindberg, J., Gazzara, M.R., Mallory, M.J., Zhang, K., García-Sastre, A., Fontoura, B.M.A., et al. (2018). Co-regulatory activity of hnRNP K and NS1-BP in influenza and human mRNA splicing. Nat. Commun. *9*, 2407. https://doi.org/10.1038/s41467-018-04779-4.

8. Tsai, P.-L., Chiou, N.-T., Kuss, S., García-Sastre, A., Lynch, K.W., and Fontoura, B.M.A. (2013). Cellular RNA Binding Proteins NS1-BP and hnRNP K Regulate Influenza A Virus RNA Splicing. PLOS Pathog. *9*, e1003460. https://doi.org/10.1371/journal.ppat.1003460.

9. Mor, A., White, A., Zhang, K., Thompson, M., Esparza, M., Muñoz-Moreno, R., Koide, K., Lynch, K.W., García-Sastre, A., and Fontoura, B.M.A. (2016). Influenza virus mRNA trafficking through host nuclear speckles. Nat. Microbiol. *1*, 1–13. https://doi.org/10.1038/nmicrobiol.2016.69.

10. Jagger, B.W., Wise, H.M., Kash, J.C., Walters, K.-A., Wills, N.M., Xiao, Y.-L., Dunfee, R.L., Schwartzman, L.M., Ozinsky, A., Bell, G.L., et al. (2012). An overlapping protein-coding region in influenza A virus segment 3 modulates the host response. Science *337*, 199–204. https://doi.org/10.1126/science.1222213.

11. Gaucherand, L., Iyer, A., Gilabert, I., Rycroft, C.H., and Gaglia, M.M. (2023). Cut site preference allows influenza A virus PA-X to discriminate between host and viral mRNAs. Nat. Microbiol. *8*, 1304–1317. https://doi.org/10.1038/s41564-023-01409-8.

12. Khaperskyy, D.A., Schmaling, S., Larkins-Ford, J., McCormick, C., and Gaglia, M.M. (2016). Selective Degradation of Host RNA Polymerase II Transcripts by Influenza A Virus PA-X Host Shutoff Protein. PLOS Pathog. *12*, e1005427. https://doi.org/10.1371/journal.ppat.1005427.

13. Caudron-Herger, M., and Rippe, K. (2012). Nuclear architecture by RNA. Curr. Opin. Genet. Dev. *22*, 179–187. https://doi.org/10.1016/j.gde.2011.12.005.

14. Martin, K., and Helenius, A. (1991). Nuclear transport of influenza virus ribonucleoproteins: the viral matrix protein (M1) promotes export and inhibits import. Cell *67*, 117–130. https://doi.org/10.1016/0092-8674(91)90576-k.

15. O'Neill, R.E., Talon, J., and Palese, P. (1998). The influenza virus NEP (NS2 protein) mediates the nuclear export of viral ribonucleoproteins. EMBO J. *17*, 288–296. https://doi.org/10.1093/emboj/17.1.288.

16. Eisfeld, A.J., Kawakami, E., Watanabe, T., Neumann, G., and Kawaoka, Y. (2011). RAB11A is essential for transport of the influenza virus genome to the plasma membrane. J. Virol. *85*, 6117–6126. https://doi.org/10.1128/JVI.00378-11.

17. de Castro Martin, I.F., Fournier, G., Sachse, M., Pizarro-Cerda, J., Risco, C., and Naffakh, N. (2017). Influenza virus genome reaches the plasma membrane via a modified endoplasmic reticulum and Rab11-dependent vesicles. Nat. Commun. *8*, 1396. https://doi.org/10.1038/s41467-017-01557-6.

18. Tafesse, F.G., Sanyal, S., Ashour, J., Guimaraes, C.P., Hermansson, M., Somerharju, P., and Ploegh, H.L. (2013). Intact sphingomyelin biosynthetic pathway is essential for intracellular transport of influenza virus glycoproteins. Proc. Natl. Acad. Sci. U. S. A. *110*, 6406–6411. https://doi.org/10.1073/pnas.1219909110.

19. Watanabe, T., Kawakami, E., Shoemaker, J.E., Lopes, T.J.S., Matsuoka, Y., Tomita, Y., Kozuka-Hata, H., Gorai, T., Kuwahara, T., Takeda, E., et al. (2014). Influenza virus-host interactome screen as a platform for antiviral drug development. Cell Host Microbe *16*, 795–805. https://doi.org/10.1016/j.chom.2014.11.002.

20. Shapira, S.D., Gat-Viks, I., Shum, B.O.V., Dricot, A., de Grace, M.M., Wu, L., Gupta, P.B., Hao, T., Silver, S.J., Root, D.E., et al. (2009). A Physical and Regulatory Map of Host-Influenza Interactions Reveals Pathways in H1N1 Infection. Cell *139*, 1255–1267. https://doi.org/10.1016/j.cell.2009.12.018.

21. Haas, K.M., McGregor, M.J., Bouhaddou, M., Polacco, B.J., Kim, E.-Y., Nguyen, T.T., Newton, B.W., Urbanowski, M., Kim, H., Williams, M.A.P., et al. (2023). Proteomic and genetic analyses of influenza A viruses identify pan-viral host targets. Nat. Commun. *14*, 6030. https://doi.org/10.1038/s41467-023-41442-z.

22. Zhu, P., Liang, L., Shao, X., Luo, W., Jiang, S., Zhao, Q., Sun, N., Zhao, Y., Li, J., Wang, J., et al. (2017). Host Cellular Protein TRAPPC6AΔ Interacts with Influenza A Virus M2 Protein and Regulates Viral Propagation by Modulating M2 Trafficking. J. Virol. *91*, e01757-16. https://doi.org/10.1128/JVI.01757-16.

23. Generous, A., Thorson, M., Barcus, J., Jacher, J., Busch, M., and Sleister, H. (2014). Identification of putative interactions between swine and human influenza A virus nucleoprotein and human host proteins. Virol. J. *11*, 228. https://doi.org/10.1186/s12985-014-0228-6.

24. Ngamurulert, S., Limjindaporn, T., and Auewaraku, P. (2009). Identification of cellular partners of Influenza A virus (H5N1) non-structural protein NS1 by yeast two-hybrid system. Acta Virol. *53*, 153–159. https://doi.org/10.4149/av_2009_03_153.

25. Wang, L., Fu, B., Li, W., Patil, G., Liu, L., Dorf, M.E., and Li, S. (2017). Comparative influenza protein interactomes identify the role of plakophilin 2 in virus restriction. Nat. Commun. *8*, 13876. https://doi.org/10.1038/ncomms13876.

26. Dugied, G., Douche, T., Dos Santos, M., Giai Gianetto Q, Q., Cassonnet, C., Vuillier, F., Cassonnet, P., Jacob, Y., van der Werf, S., Komarova, A., et al. (2024). Profiling Cullin4-E3 Ligases Interactomes and Their Rewiring in Influenza A Virus Infection. Mol. Cell. Proteomics MCP *23*, 100856. https://doi.org/10.1016/j.mcpro.2024.100856.

27. Bradel-Tretheway, B.G., Mattiacio, J.L., Krasnoselsky, A., Stevenson, C., Purdy, D., Dewhurst, S., and Katze, M.G. (2011). Comprehensive proteomic analysis of influenza virus polymerase complex reveals a novel association with mitochondrial proteins and RNA polymerase accessory factors. J. Virol. *85*, 8569–8581. https://doi.org/10.1128/JVI.00496-11.

28. Martin-Sancho, L., Tripathi, S., Rodriguez-Frandsen, A., Pache, L., Sanchez-Aparicio, M., McGregor, M.J., Haas, K.M., Swaney, D.L., Nguyen, T.T., Mamede, J.I., et al. (2021). Restriction factor compendium for influenza A virus reveals a mechanism for evasion of autophagy. Nat. Microbiol. *6*, 1319–1333. https://doi.org/10.1038/s41564-021-00964-2.

29. Bogdanow, B., Mühlberg, L., Gruska, I., Vetter, B., Ruta, J., Elofsson, A., Wiebusch, L., and Liu, F. (2023). Structural Host-Virus Interactome Profiling of Intact Infected Cells. Preprint at bioRxiv, https://doi.org/10.1101/2023.12.03.569778 https://doi.org/10.1101/2023.12.03.569778.

30. Bogdanow, B., Wang, X., Eichelbaum, K., Sadewasser, A., Husic, I., Paki, K., Budt, M., Hergeselle, M., Vetter, B., Hou, J., et al. (2019). The dynamic proteome of influenza A virus infection identifies M segment splicing as a host range determinant. Nat. Commun. *10*, 5518. https://doi.org/10.1038/s41467-019-13520-8.

31. Hutchinson, E.C., and Fodor, E. (2013). Transport of the Influenza Virus Genome from Nucleus to Nucleus. Viruses *5*, 2424–2446. https://doi.org/10.3390/v5102424.

32. Bartolec, T.K., Vázquez-Campos, X., Norman, A., Luong, C., Johnson, M., Payne, R.J., Wilkins, M.R., Mackay, J.P., and Low, J.K.K. (2023). Cross-linking mass spectrometry discovers, evaluates, and corroborates structures and protein–protein interactions in the human cell. Proc. Natl. Acad. Sci. *120*, e2219418120. https://doi.org/10.1073/pnas.2219418120.

33. Soonthornvacharin, S., Rodriguez-Frandsen, A., Zhou, Y., Galvez, F., Huffmaster, N.J., Tripathi, S., Balasubramaniam, V.R.M.T., Inoue, A., de Castro, E., Moulton, H., et al. (2017). Systems-based analysis of RIG-I-dependent signalling identifies KHSRP as an inhibitor of RIG-I receptor activation. Nat. Microbiol. *2*, 17022. https://doi.org/10.1038/nmicrobiol.2017.22.

34. Dupont, M., Krischuns, T., Gianetto, Q.G., Paisant, S., Bonazza, S., Brault, J.-B., Douché, T., Arragain, B., Florez-Prada, A., Perez-Perri, J.I., et al. (2024). The RBPome of influenza A virus NP-mRNA reveals a role for TDP-43 in viral replication. Nucleic Acids Res. *52*, 7188–7210. https://doi.org/10.1093/nar/gkae291.

35. Nilsson-Payant, B.E., tenOever, B.R., and Te Velthuis, A.J.W. (2022). The Host Factor ANP32A Is Required for Influenza A Virus vRNA and cRNA Synthesis. J. Virol. *96*, e0209221. https://doi.org/10.1128/jvi.02092-21.

36. Zhirnov, O.P., and Klenk, H.D. (1997). Histones as a target for influenza virus matrix protein M1. Virology *235*, 302–310. https://doi.org/10.1006/viro.1997.8700.

37. Garcia-Robles, I., Akarsu, H., Müller, C.W., Ruigrok, R.W.H., and Baudin, F. (2005). Interaction of influenza virus proteins with nucleosomes. Virology *332*, 329–336. https://doi.org/10.1016/j.virol.2004.09.036.

38. Avalos, R.T., Yu, Z., and Nayak, D.P. (1997). Association of influenza virus NP and M1 proteins with cellular cytoskeletal elements in influenza virus-infected cells. J. Virol. *71*, 2947–2958. https://doi.org/10.1128/JVI.71.4.2947-2958.1997.

39. Fislová, T., Thomas, B., Graef, K.M., and Fodor, E. (2010). Association of the Influenza Virus RNA Polymerase Subunit PB2 with the Host Chaperonin CCT. J. Virol. *84*, 8691–8699. https://doi.org/10.1128/jvi.00813-10.

40. Chua, S.C.J.H., Cui, J., Engelberg, D., and Lim, L.H.K. (2022). A Review and Meta-Analysis of Influenza Interactome Studies. Front. Microbiol. *13*.

41. O'Reilly, F.J., and Rappsilber, J. (2018). Cross-linking mass spectrometry: methods and applications in structural, molecular and systems biology. Nat. Struct. Mol. Biol. *25*, 1000–1008. https://doi.org/10.1038/s41594-018-0147-0.

42. te Velthuis, A.J.W., Grimes, J.M., and Fodor, E. (2021). Structural insights into RNA polymerases of negative-sense RNA viruses. Nat. Rev. Microbiol. *19*, 303–318. https://doi.org/10.1038/s41579-020-00501-8.

43. Thierry, E., Guilligay, D., Kosinski, J., Bock, T., Gaudon, S., Round, A., Pflug, A., Hengrung, N., El Omari, K., Baudin, F., et al. (2016). Influenza Polymerase Can Adopt an Alternative Configuration Involving a Radical Repacking of PB2 Domains. Mol. Cell *61*, 125–137. https://doi.org/10.1016/j.molcel.2015.11.016.

44. Jumper, J., Evans, R., Pritzel, A., Green, T., Figurnov, M., Ronneberger, O., Tunyasuvunakool, K., Bates, R., Žídek, A., Potapenko, A., et al. (2021). Highly accurate protein structure prediction with AlphaFold. Nature *596*, 583–589. https://doi.org/10.1038/s41586-021-03819-2.

45. Evans, R., O'Neill, M., Pritzel, A., Antropova, N., Senior, A., Green, T., Žídek, A., Bates, R., Blackwell, S., Yim, J., et al. (2022). Protein complex prediction with AlphaFold-Multimer. Preprint at bioRxiv, https://doi.org/10.1101/2021.10.04.463034 https://doi.org/10.1101/2021.10.04.463034.

46. Abramson, J., Adler, J., Dunger, J., Evans, R., Green, T., Pritzel, A., Ronneberger, O., Willmore, L., Ballard, A.J., Bambrick, J., et al. (2024). Accurate structure prediction of biomolecular interactions with AlphaFold 3. Nature *630*, 493–500. https://doi.org/10.1038/s41586-024-07487-w.

47. Kosinski, J. (2024). Improving AlphaFold 3 structural modeling by incorporating explicit crosslinks. Preprint at bioRxiv, https://doi.org/10.1101/2024.12.03.626671 https://doi.org/10.1101/2024.12.03.626671.

48. Diot, C., Fournier, G., Dos Santos, M., Magnus, J., Komarova, A., van der Werf, S., Munier, S., and Naffakh, N. (2016). Influenza A Virus Polymerase Recruits the RNA Helicase DDX19 to Promote the Nuclear Export of Viral mRNAs. Sci. Rep. *6*, 33763. https://doi.org/10.1038/srep33763.

49. Veler, H., Fan, H., Keown, J.R., Sharps, J., Fournier, M., Grimes, J.M., and Fodor, E. (2022). The C-Terminal Domains of the PB2 Subunit of the Influenza A Virus RNA Polymerase Directly Interact with Cellular GTPase Rab11a. J. Virol. *96*, e01979-21. https://doi.org/10.1128/jvi.01979-21.

50. de la Luna, S., Fortes, P., Beloso, A., and Ortín, J. (1995). Influenza virus NS1 protein enhances the rate of translation initiation of viral mRNAs. J. Virol. *69*, 2427–2433.

51. Scalise, M., Galluccio, M., Console, L., Pochini, L., and Indiveri, C. (2018). The Human SLC7A5 (LAT1): The Intriguing Histidine/Large Neutral Amino Acid Transporter and Its Relevance to Human Health. Front. Chem. *6*. https://doi.org/10.3389/fchem.2018.00243.

52. Tae, K., Kim, S.-J., Cho, S.-W., Lee, H., Cha, H.-S., and Choi, C.-Y. (2023). L-Type Amino Acid Transporter 1 (LAT1) Promotes PMA-Induced Cell Migration through mTORC2 Activation at the Lysosome. Cells *12*, 2504. https://doi.org/10.3390/cells12202504.

53. Böttcher-Friebertshäuser, E., Klenk, H.-D., and Garten, W. (2013). Activation of influenza viruses by proteases from host cells and bacteria in the human airway epithelium. Pathog. Dis. *69*, 87–100. https://doi.org/10.1111/2049-632X.12053.

54. Copeland, C.S., Doms, R.W., Bolzau, E.M., Webster, R.G., and Helenius, A. (1986). Assembly of influenza hemagglutinin trimers and its role in intracellular transport. J. Cell Biol. *103*, 1179–1191. https://doi.org/10.1083/jcb.103.4.1179.

55. Matlin, K.S., and Simons, K. (1983). Reduced temperature prevents transfer of a membrane glycoprotein to the cell surface but does not prevent terminal glycosylation. Cell *34*, 233–243. https://doi.org/10.1016/0092-8674(83)90154-x.

56. Rodriguez-Boulan, E., Paskiet, K.T., Salas, P.J., and Bard, E. (1984). Intracellular transport of influenza virus hemagglutinin to the apical surface of Madin-Darby canine kidney cells. J. Cell Biol. *98*, 308–319. https://doi.org/10.1083/jcb.98.1.308.

57. Kozlov, G., and Gehring, K. (2020). Calnexin cycle - structural features of the ER chaperone system. FEBS J. *287*, 4322–4340. https://doi.org/10.1111/febs.15330.

58. Hebert, D.N., Foellmer, B., and Helenius, A. (1996). Calnexin and calreticulin promote folding, delay oligomerization and suppress degradation of influenza hemagglutinin in microsomes. EMBO J. *15*, 2961–2968.

59. Hebert, D.N., Zhang, J.X., Chen, W., Foellmer, B., and Helenius, A. (1997). The number and location of glycans on influenza hemagglutinin determine folding and association with calnexin and calreticulin. J. Cell Biol. *139*, 613–623. https://doi.org/10.1083/jcb.139.3.613.

60. Molinari, M., Eriksson, K.K., Calanca, V., Galli, C., Cresswell, P., Michalak, M., and Helenius, A. (2004). Contrasting functions of calreticulin and calnexin in glycoprotein folding and ER quality control. Mol. Cell *13*, 125–135. https://doi.org/10.1016/s1097-2765(03)00494-5.

61. Chamberlain, N., Korwin-Mihavics, B.R., Nakada, E.M., Bruno, S.R., Heppner, D.E., Chapman, D.G., Hoffman, S.M., van der Vliet, A., Suratt, B.T., Dienz, O., et al. (2019). Lung epithelial protein disulfide isomerase A3 (PDIA3) plays an important role in influenza infection, inflammation, and airway mechanics. Redox Biol. *22*, 101129. https://doi.org/10.1016/j.redox.2019.101129.

62. Soldà, T., Garbi, N., Hämmerling, G.J., and Molinari, M. (2006). Consequences of ERp57 deletion on oxidative folding of obligate and facultative clients of the calnexin cycle. J. Biol. Chem. *281*, 6219–6226. https://doi.org/10.1074/jbc.M513595200.

63. Brecker, M., Khakhina, S., Schubert, T.J., Thompson, Z., and Rubenstein, R.C. (2020). The Probable, Possible, and Novel Functions of ERp29. Front. Physiol. *11*, 574339. https://doi.org/10.3389/fphys.2020.574339.

64. Füllekrug, J., Scheiffele, P., and Simons, K. (1999). VIP36 localisation to the early secretory pathway. J. Cell Sci. *112 (Pt 17)*, 2813–2821. https://doi.org/10.1242/jcs.112.17.2813.

65. Hara-Kuge, S., Ohkura, T., Seko, A., and Yamashita, K. (1999). Vesicular-integral membrane protein, VIP36, recognizes high-mannose type glycans containing alpha1-->2 mannosyl residues in MDCK cells. Glycobiology *9*, 833–839. https://doi.org/10.1093/glycob/9.8.833.

66. Klaus, J.P., Eisenhauer, P., Russo, J., Mason, A.B., Do, D., King, B., Taatjes, D., Cornillez-Ty, C., Boyson, J.E., Thali, M., et al. (2013). The intracellular cargo receptor ERGIC-53 is required for the production of infectious arenavirus, coronavirus, and filovirus particles. Cell Host Microbe *14*, 522–534. https://doi.org/10.1016/j.chom.2013.10.010.

67. Kwon, S.-H., Oh, S., Nacke, M., Mostov, K.E., and Lipschutz, J.H. (2016). Adaptor Protein CD2AP and L-type Lectin LMAN2 Regulate Exosome Cargo Protein Trafficking through the Golgi Complex. J. Biol. Chem. *291*, 25462–25475. https://doi.org/10.1074/jbc.M116.729202.

68. Clark, C.R., Maile, M., Blaney, P., Hellweg, S.R., Strauss, A., Durose, W., Priya, S., Habicht, J., Burns, M.B., Blekhman, R., et al. (2018). Transposon mutagenesis screen in mice identifies TM9SF2 as a novel colorectal cancer oncogene. Sci. Rep. *8*, 15327. https://doi.org/10.1038/s41598-018-33527-3.

69. Schimmöller, F., Díaz, E., Mühlbauer, B., and Pfeffer, S.R. (1998). Characterization of a 76 kDa endosomal, multispanning membrane protein that is highly conserved throughout evolution. Gene *216*, 311–318. https://doi.org/10.1016/s0378-1119(98)00349-7.

70. Bell, A.W., Ward, M.A., Blackstock, W.P., Freeman, H.N., Choudhary, J.S., Lewis, A.P., Chotai, D., Fazel, A., Gushue, J.N., Paiement, J., et al. (2001). Proteomics characterization of abundant Golgi membrane proteins. J. Biol. Chem. *276*, 5152–5165. https://doi.org/10.1074/jbc.M006143200.

71. Pacheco, A.R., Lazarus, J.E., Sit, B., Schmieder, S., Lencer, W.I., Blondel, C.J., Doench, J.G., Davis, B.M., and Waldor, M.K. (2018). CRISPR Screen Reveals that EHEC's T3SS and Shiga Toxin Rely on Shared Host Factors for Infection. mBio *9*, e01003-18. https://doi.org/10.1128/mBio.01003-18.

72. Tian, S., Muneeruddin, K., Choi, M.Y., Tao, L., Bhuiyan, R.H., Ohmi, Y., Furukawa, K., Furukawa, K., Boland, S., Shaffer, S.A., et al. (2018). Genome-wide CRISPR screens for Shiga toxins and ricin reveal Golgi proteins critical for glycosylation. PLoS Biol. *16*, e2006951. https://doi.org/10.1371/journal.pbio.2006951.

73. Heaton, B.E., Kennedy, E.M., Dumm, R.E., Harding, A.T., Sacco, M.T., Sachs, D., and Heaton, N.S. (2017). A CRISPR Activation Screen Identifies a Pan-avian Influenza Virus Inhibitory Host Factor. Cell Rep. *20*, 1503–1512. https://doi.org/10.1016/j.celrep.2017.07.060.

74. Fox, A.H., Nakagawa, S., Hirose, T., and Bond, C.S. (2018). Paraspeckles: Where Long Noncoding RNA Meets Phase Separation. Trends Biochem. Sci. *43*, 124–135. https://doi.org/10.1016/j.tibs.2017.12.001.

75. Hirose, T., Virnicchi, G., Tanigawa, A., Naganuma, T., Li, R., Kimura, H., Yokoi, T., Nakagawa, S., Bénard, M., Fox, A.H., et al. (2014). NEAT1 long noncoding RNA regulates transcription via protein sequestration within subnuclear bodies. Mol. Biol. Cell *25*, 169–183. https://doi.org/10.1091/mbc.e13-09-0558.

76. Hirose, T., Yamazaki, T., and Nakagawa, S. (2019). Molecular anatomy of the architectural NEAT1 noncoding RNA: The domains, interactors, and biogenesis pathway required to build phase-separated nuclear paraspeckles. WIREs RNA *10*, e1545. https://doi.org/10.1002/wrna.1545.

77. Naganuma, T., and Hirose, T. (2013). Paraspeckle formation during the biogenesis of long non-coding RNAs. RNA Biol. *10*, 456–461. https://doi.org/10.4161/rna.23547.

78. Clemson, C.M., Hutchinson, J.N., Sara, S.A., Ensminger, A.W., Fox, A.H., Chess, A., and Lawrence, J.B. (2009). An Architectural Role for a Nuclear Non-coding RNA: NEAT1 RNA is Essential for the Structure of Paraspeckles. Mol. Cell *33*, 717–726. https://doi.org/10.1016/j.molcel.2009.01.026.

79. Takakuwa, H., Yamazaki, T., Souquere, S., Adachi, S., Yoshino, H., Fujiwara, N., Yamamoto, T., Natsume, T., Nakagawa, S., Pierron, G., et al. (2023). Shell protein composition specified by the lncRNA NEAT1 domains dictates the formation of paraspeckles as distinct membraneless organelles. Nat. Cell Biol. *25*, 1664–1675. https://doi.org/10.1038/s41556-023-01254-1.

80. Fox, A.H., Lam, Y.W., Leung, A.K.L., Lyon, C.E., Andersen, J., Mann, M., and Lamond, A.I. (2002). Paraspeckles: A Novel Nuclear Domain. Curr. Biol. *12*, 13–25. https://doi.org/10.1016/S0960-9822(01)00632-7.

81. Fox, A.H., Bond, C.S., and Lamond, A.I. (2005). P54nrb Forms a Heterodimer with PSP1 That Localizes to Paraspeckles in an RNA-dependent Manner. Mol. Biol. Cell *16*, 5304–5315. https://doi.org/10.1091/mbc.e05-06-0587.

82. Knott, G.J., Bond, C.S., and Fox, A.H. (2016). The DBHS proteins SFPQ, NONO and PSPC1: a multipurpose molecular scaffold. Nucleic Acids Res. *44*, 3989–4004. https://doi.org/10.1093/nar/gkw271.

83. Hennig, S., Kong, G., Mannen, T., Sadowska, A., Kobelke, S., Blythe, A., Knott, G.J., Iyer, K.S., Ho, D., Newcombe, E.A., et al. (2015). Prion-like domains in RNA binding proteins are essential for building subnuclear paraspeckles. J. Cell Biol. *210*, 529–539. https://doi.org/10.1083/jcb.201504117.

84. Prasanth, K.V., Prasanth, S.G., Xuan, Z., Hearn, S., Freier, S.M., Bennett, C.F., Zhang, M.Q., and Spector, D.L. (2005). Regulating Gene Expression through RNA Nuclear Retention. Cell *123*, 249–263. https://doi.org/10.1016/j.cell.2005.08.033.

85. Imamura, K., Imamachi, N., Akizuki, G., Kumakura, M., Kawaguchi, A., Nagata, K., Kato, A., Kawaguchi, Y., Sato, H., Yoneda, M., et al. (2014). Long Noncoding RNA NEAT1-Dependent SFPQ Relocation from Promoter Region to Paraspeckle

Mediates IL8 Expression upon Immune Stimuli. Mol. Cell *53*, 393–406. https://doi.org/10.1016/j.molcel.2014.01.009.

86. Landeras-Bueno, S., Jorba, N., Pérez-Cidoncha, M., and Ortín, J. (2011). The Splicing Factor Proline-Glutamine Rich (SFPQ/PSF) Is Involved in Influenza Virus Transcription. PLOS Pathog. *7*, e1002397. https://doi.org/10.1371/journal.ppat.1002397.

87. Beyleveld, G., Chin, D.J., Moreno Del Olmo, E., Carter, J., Najera, I., Cillóniz, C., and Shaw, M.L. (2018). Nucleolar Relocalization of RBM14 by Influenza A Virus NS1 Protein. mSphere *3*, e00549-18. https://doi.org/10.1128/mSphereDirect.00549-18.

88. Kaur, R., Batra, J., Stuchlik, O., Reed, M.S., Pohl, J., Sambhara, S., and Lal, S.K. (2022). Heterogeneous Ribonucleoprotein A1 (hnRNPA1) Interacts with the Nucleoprotein of the Influenza a Virus and Impedes Virus Replication. Viruses *14*, 199. https://doi.org/10.3390/v14020199.

89. Lv, L., Yang, X., Zhang, Y., Ren, X., Zeng, S., Zhang, Z., Wang, Q., Lv, J., Gao, P., Dorf, M.E., et al. (2024). hnRNPAB inhibits Influenza A virus infection by disturbing polymerase activity. Antiviral Res. *228*, 105925. https://doi.org/10.1016/j.antiviral.2024.105925.

90. Tang, Y.-S., So, W.-K., Ng, K.-L.A., Mok, K.-P.C., and Shaw, P.-C. (2022). Interaction of Influenza A Nucleoprotein with Host hnRNP-C Is Implicated in Viral Replication. Int. J. Mol. Sci. *23*, 13613. https://doi.org/10.3390/ijms232113613.

91. Wang, X., Lin, L., Zhong, Y., Feng, M., Yu, T., Yan, Y., Zhou, J., and Liao, M. (2021). Cellular hnRNPAB binding to viral nucleoprotein inhibits flu virus replication by blocking nuclear export of viral mRNA. iScience *24*, 102160. https://doi.org/10.1016/j.isci.2021.102160.

92. Ye, H., Bi, Z., Fan, W., Song, S., and Yan, L. (2021). Cellular hnRNPAB interacts with avian influenza viral protein PB2 and inhibits virus replication potentially by restricting PB2 mRNA nuclear export and PB2 protein level. Virus Res. *305*, 198573. https://doi.org/10.1016/j.virusres.2021.198573.

93. Chan, A.Y., Vreede, F.T., Smith, M., Engelhardt, O.G., and Fodor, E. (2006). Influenza virus inhibits RNA polymerase II elongation. Virology *351*, 210–217. https://doi.org/10.1016/j.virol.2006.03.005.

94. Vreede, F.T., Chan, A.Y., Sharps, J., and Fodor, E. (2010). Mechanisms and functional implications of the degradation of host RNA polymerase II in influenza virus infected cells. Virology *396*, 125–134. https://doi.org/10.1016/j.virol.2009.10.003.

95. Vreede, F.T., and Fodor, E. (2010). The role of the influenza virus RNA polymerase in host shut-off. Virulence *1*, 436–439. https://doi.org/10.4161/viru.1.5.12967.

96. Vetter, J. (1998). Toxins of Amanita phalloides. Toxicon Off. J. Int. Soc. Toxinology *36*, 13–24. https://doi.org/10.1016/s0041-0101(97)00074-3.

97. Kawakami, E., Watanabe, T., Fujii, K., Goto, H., Watanabe, S., Noda, T., and Kawaoka, Y. (2011). Strand-specific real-time RT-PCR for distinguishing influenza vRNA, cRNA, and mRNA. J. Virol. Methods *173*, 1–6. https://doi.org/10.1016/j.jviromet.2010.12.014.

98. Yamazaki, T., Souquere, S., Chujo, T., Kobelke, S., Chong, Y.S., Fox, A.H., Bond, C.S., Nakagawa, S., Pierron, G., and Hirose, T. (2018). Functional Domains of NEAT1 Architectural lncRNA Induce Paraspeckle Assembly through Phase Separation. Mol. Cell *70*, 1038-1053.e7. https://doi.org/10.1016/j.molcel.2018.05.019.

99. Wang, Z., Qiu, H., He, J., Liu, L., Xue, W., Fox, A., Tickner, J., and Xu, J. (2020). The emerging roles of hnRNPK. J. Cell. Physiol. *235*, 1995–2008. https://doi.org/10.1002/jcp.29186.

100. Coelho, M.B., Attig, J., Bellora, N., König, J., Hallegger, M., Kayikci, M., Eyras, E., Ule, J., and Smith, C.W. (2015). Nuclear matrix protein Matrin3 regulates alternative splicing and forms overlapping regulatory networks with PTB. EMBO J. *34*, 653–668. https://doi.org/10.15252/embj.201489852.

101. Krecic, A.M., and Swanson, M.S. (1999). hnRNP complexes: composition, structure, and function. Curr. Opin. Cell Biol. *11*, 363–371. https://doi.org/10.1016/S0955-0674(99)80051-9.

102. Wolff, T., O'Neill, R.E., and Palese, P. (1998). NS1-Binding protein (NS1-BP): a novel human protein that interacts with the influenza A virus nonstructural NS1 protein is relocalized in the nuclei of infected cells. J. Virol. *72*, 7170–7180. https://doi.org/10.1128/JVI.72.9.7170-7180.1998.

103. Krischuns, T., Arragain, B., Isel, C., Paisant, S., Budt, M., Wolff, T., Cusack, S., and Naffakh, N. (2024). The host RNA polymerase II C-terminal domain is the anchor for replication of the influenza virus genome. Nat. Commun. *15*, 1064. https://doi.org/10.1038/s41467-024-45205-2.

104. Keown, J., Baazaoui, A., Šebesta, M., Štefl, R., Carrique, L., Fodor, E., and Grimes, J.M. (2024). Structural and functional characterization of the interaction between the influenza A virus RNA polymerase and the CTD of host RNA polymerase II. J. Virol. *98*, e00138-24. https://doi.org/10.1128/jvi.00138-24.

105. Sheppard, C.M., Goldhill, D.H., Swann, O.C., Staller, E., Penn, R., Platt, O.K., Sukhova, K., Baillon, L., Frise, R., Peacock, T.P., et al. (2023). An Influenza A virus can evolve to use human ANP32E through altering polymerase dimerization. Nat. Commun. *14*, 6135. https://doi.org/10.1038/s41467-023-41308-4.

106. Staller, E., Carrique, L., Swann, O.C., Fan, H., Keown, J.R., Sheppard, C.M., Barclay, W.S., Grimes, J.M., and Fodor, E. (2024). Structures of H5N1 influenza polymerase with ANP32B reveal mechanisms of genome replication and host adaptation. Nat. Commun. *15*, 4123. https://doi.org/10.1038/s41467-024-48470-3.

107. Li, W., He, Y., Yang, J., Hu, G., Lin, Y., Ran, T., Peng, B., Xie, B., Huang, M., Gao, X., et al. (2021). Profiling PRMT methylome reveals roles of hnRNPA1 arginine methylation in RNA splicing and cell growth. Nat. Commun. *12*, 1946. https://doi.org/10.1038/s41467-021-21963-1.

108. Liu, N., Dai, Q., Zheng, G., He, C., Parisien, M., and Pan, T. (2015). N6-methyladenosine-dependent RNA structural switches regulate RNA–protein interactions. Nature *518*, 560–564. https://doi.org/10.1038/nature14234.

109. Azam, S., Armijo, K.S., Weindel, C.G., Chapman, M.J., Devigne, A., Nakagawa, S., Hirose, T., Carpenter, S., Watson, R.O., and Patrick, K.L. (2024). The early macrophage response to pathogens requires dynamic regulation of the nuclear paraspeckle. Proc. Natl. Acad. Sci. U. S. A. *121*, e2312587121. https://doi.org/10.1073/pnas.2312587121.

110. Ingram, H.B., and Fox, A.H. (2024). Unveiling the intricacies of paraspeckle formation and function. Curr. Opin. Cell Biol. *90*, 102399. https://doi.org/10.1016/j.ceb.2024.102399.

111. Rodriguez-Frandsen, A., Martin-Sancho, L., Gounder, A.P., Chang, M.W., Liu, W.-C., De Jesus, P.D., von Recum-Knepper, J., Dutra, M.S., Huffmaster, N.J., Chavarria, M., et al. (2020). Viral Determinants in H5N1 Influenza A Virus Enable Productive Infection of HeLa Cells. J. Virol. *94*, 10.1128/jvi.01410-19. https://doi.org/10.1128/jvi.01410-19.

112. Gujuluva, C.N., Kundu, A., Murti, K.G., and Nayak, D.P. (1994). Abortive Replication of Influenza Virus A/WSN/33 in HeLa229 Cells: Defective Viral Entry and Budding Processes. Virology *204*, 491–505. https://doi.org/10.1006/viro.1994.1563.

113. Ludwig, S., Ehrhardt, C., Neumeier, E.R., Kracht, M., Rapp, U.R., and Pleschka, S. (2001). Influenza Virus-induced AP-1-dependent Gene Expression Requires Activation of the JNK Signaling Pathway*. J. Biol. Chem. *276*, 10990–10998. https://doi.org/10.1074/jbc.M009902200.

114. Lerner, R.A., and Hodge, L.D. (1969). NONPERMISSIVE INFECTIONS OF MAMMALIAN CELLS: SYNTHESIS OF INFLUENZA VIRUS GENOME IN HeLa CELLS*. Proc. Natl. Acad. Sci. *64*, 544–551. https://doi.org/10.1073/pnas.64.2.544.

115. Portincasa, P., Conti, G., and Chezzi, C. (1990). Abortive replication of influenza A viruses in HeLa 229 cells. Virus Res. *18*, 29–40. https://doi.org/10.1016/0168-1702(90)90087-r.

116. Friedl, M.-S., Djakovic, L., Kluge, M., Hennig, T., Whisnant, A.W., Backes, S., Dölken, L., and Friedel, C.C. (2022). HSV-1 and influenza infection induce linear and circular splicing of the long NEAT1 isoform. PLOS ONE *17*, e0276467. https://doi.org/10.1371/journal.pone.0276467.

117. Ma, H., Han, P., Ye, W., Chen, H., Zheng, X., Cheng, L., Zhang, L., Yu, L., Wu, X., Xu, Z., et al. (2017). The Long Noncoding RNA NEAT1 Exerts Antihantaviral

Effects by Acting as Positive Feedback for RIG-I Signaling. J. Virol. *91*, 10.1128/jvi.02250-16. https://doi.org/10.1128/jvi.02250-16.

118. Wang, Z., Fan, P., Zhao, Y., Zhang, S., Lu, J., Xie, W., Jiang, Y., Lei, F., Xu, N., and Zhang, Y. (2017). NEAT1 modulates herpes simplex virus-1 replication by regulating viral gene transcription. Cell. Mol. Life Sci. CMLS *74*, 1117–1131. https://doi.org/10.1007/s00018-016-2398-4.

119. Saini, J., Thapa, U., Bandyopadhyay, B., Vrati, S., and Banerjee, A. (2023). Knockdown of NEAT1 restricts dengue virus replication by augmenting interferon alpha-inducible protein 27 via the RIG-I pathway. J. Gen. Virol. *104*, 001823. https://doi.org/10.1099/jgv.0.001823.

120. Ni, Z., Wang, J., Yu, X., Wang, Y., Wang, J., He, X., Li, C., Deng, G., Shi, J., Kong, H., et al. (2024). Influenza virus uses mGluR2 as an endocytic receptor to enter cells. Nat. Microbiol. *9*, 1764–1777. https://doi.org/10.1038/s41564-024-01713-x.

121. Rappsilber, J., Ishihama, Y., and Mann, M. (2003). Stop and go extraction tips for matrix-assisted laser desorption/ionization, nanoelectrospray, and LC/MS sample pretreatment in proteomics. Anal. Chem. *75*, 663–670. https://doi.org/10.1021/ac026117i.

122. Wessel, D., and Flügge, U.I. (1984). A method for the quantitative recovery of protein in dilute solution in the presence of detergents and lipids. Anal. Biochem. *138*, 141–143. https://doi.org/10.1016/0003-2697(84)90782-6.

123. Cox, J., and Mann, M. (2008). MaxQuant enables high peptide identification rates, individualized p.p.b.-range mass accuracies and proteome-wide protein quantification. Nat. Biotechnol. *26*, 1367–1372. https://doi.org/10.1038/nbt.1511.

124. Bogdanow, B., Gruska, I., Mühlberg, L., Protze, J., Hohensee, S., Vetter, B., Lehmann, M., Wiebusch, L., and Liu, F. (2022). Spatial, Quantitative and Functional Deconstruction of Virus and Host Protein Interactions Inside Intact Cytomegalovirus Particles (Microbiology) https://doi.org/10.1101/2022.05.02.490278.

125. Clasen, M.A., Ruwolt, M., Wang, C., Ruta, J., Bogdanow, B., Kurt, L.U., Zhang, Z., Wang, S., Gozzo, F.C., Chen, T., et al. (2024). Proteome-scale recombinant standards and a robust high-speed search engine to advance cross-linking MS-based interactomics. Nat. Methods *21*, 2327–2335. https://doi.org/10.1038/s41592-024-02478-1.

126. The UniProt Consortium (2023). UniProt: the Universal Protein Knowledgebase in 2023. Nucleic Acids Res. *51*, D523–D531. https://doi.org/10.1093/nar/gkac1052.

127. Bittrich, S., Bhikadiya, C., Bi, C., Chao, H., Duarte, J.M., Dutta, S., Fayazi, M., Henry, J., Khokhriakov, I., Lowe, R., et al. (2023). RCSB Protein Data Bank: Efficient Searching and Simultaneous Access to One Million Computed Structure

Models Alongside the PDB Structures Enabled by Architectural Advances. J. Mol. Biol. *435*, 167994. https://doi.org/10.1016/j.jmb.2023.167994.

128. Yu, D., Chojnowski, G., Rosenthal, M., and Kosinski, J. (2023). AlphaPulldown-a python package for protein-protein interaction screens using AlphaFold-Multimer. Bioinforma. Oxf. Engl. *39*, btac749. https://doi.org/10.1093/bioinformatics/btac749.

129. Meng, E.C., Goddard, T.D., Pettersen, E.F., Couch, G.S., Pearson, Z.J., Morris, J.H., and Ferrin, T.E. (2023). UCSF ChimeraX: Tools for structure building and analysis. Protein Sci. *32*, e4792. https://doi.org/10.1002/pro.4792.

130. Kuleshov, M.V., Jones, M.R., Rouillard, A.D., Fernandez, N.F., Duan, Q., Wang, Z., Koplev, S., Jenkins, S.L., Jagodnik, K.M., Lachmann, A., et al. (2016). Enrichr: a comprehensive gene set enrichment analysis web server 2016 update. Nucleic Acids Res. *44*, W90–W97. https://doi.org/10.1093/nar/gkw377.

131. Combe, C.W., Fischer, L., and Rappsilber, J. (2015). xiNET: cross-link network maps with residue resolution. Mol. Cell. Proteomics MCP *14*, 1137–1147. https://doi.org/10.1074/mcp.O114.042259.

Supplemental Information

Video S1. NONO or SFPQ cellular localisation in A549 cells stably overexpressing mEGFP-NONO or mEGFP-SFPQ infected with WSN at MOI 3 or mock-infected and imaged every 40 min.

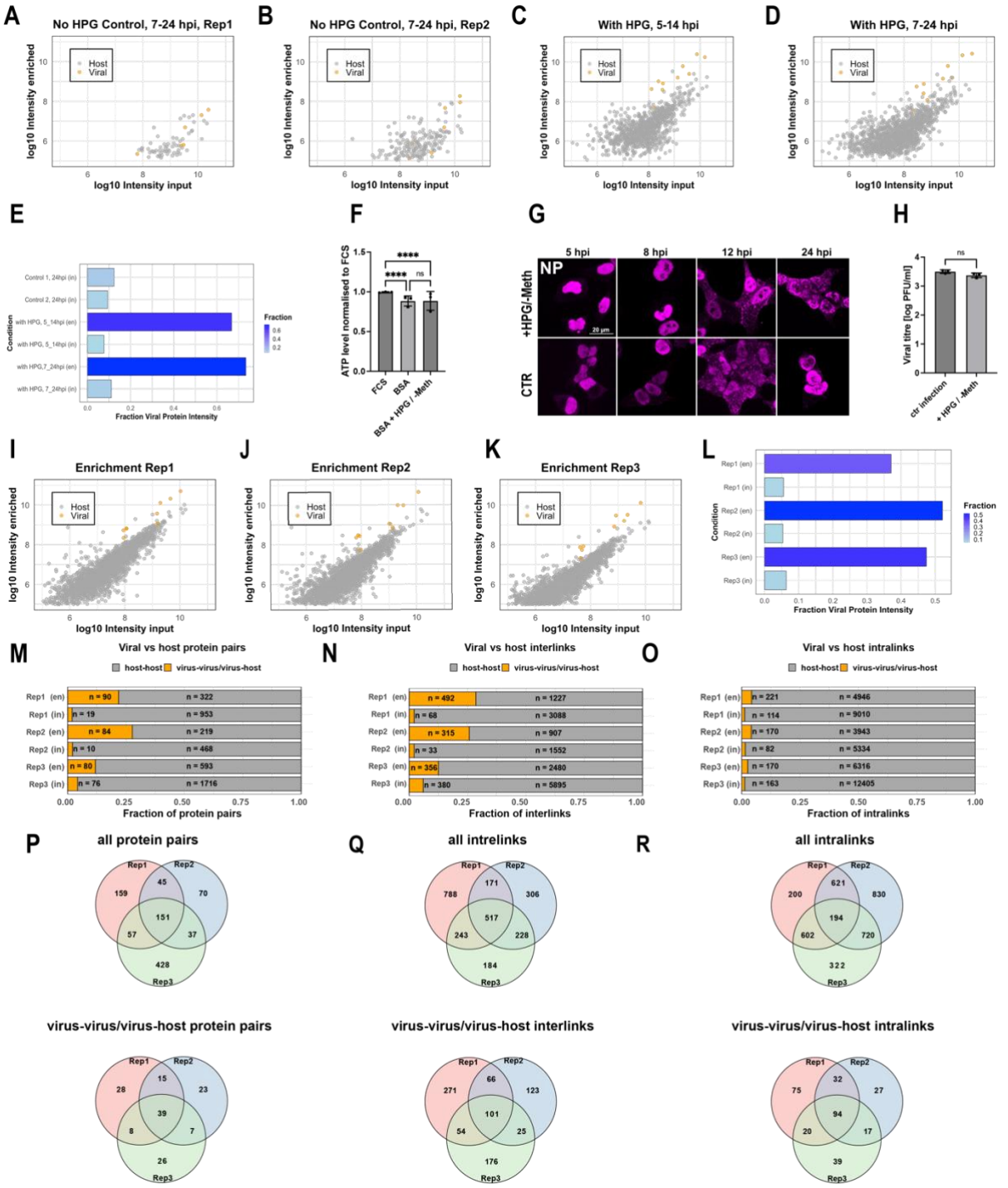

Figure S1. Optimisation of SHVIP and enrichment of IAV proteome in the SHVIP experiment.

(A-D) Determination of optimal time frames for selective enrichment of viral proteins. Scatter plots represent the correlation between input (x-axis) and enriched (y-axis) log10 iBAQ-values (intensity-based absolute quantification of proteins) of host (grey) and viral (orange) proteins at various time points and conditions. Conditions include

no-HPG controls (A-B) at 7–24 hpi and HPG-containing samples at 5–14 hpi (C) and 7–24 hpi (D). L-HPG stands for L-homopropargylglycine.

(E) Fraction of viral protein intensities in total proteomic data under various conditions summarising the data show in (A-D). Bars represent the proportion of viral proteins enriched relative to input proteins across different experimental setups. Enriched samples indicated as en, and input as in.

(F) Viability of A549 cells after incubation in three different media conditions: complete media (FCS), infectious media (BSA), and SHVIP media (BSA L-HPG). Cell viability is normalised to the complete media condition (FCS) (n=3). Data represent mean ± SD. Statistical significance was determined using an ordinary one-way ANOVA. Significance levels are indicated as follows: **** for $p < 0.0001$ and ns for not significant.

(G) Maximum projection of A549 cells infected with WSN at various time points. The viral nucleoprotein (NP) is used as an infection marker (magenta). Cells were treated with either +HPG/-Meth media or standard infectious media (CTR). Meth stands for methionine.

(H) Viral titres at 14 hpi comparing standard infectious media and +HPG/-Meth media protocols. Data represent mean ± SD (n=3). Statistical significance was determined using an ordinary one-way ANOVA. Significance levels are indicated as follows: ns for not significant.

(I-K) Scatter plots represent the correlation between input (x-axis) and enriched (y-axis) log10 iBAQ-values of host (grey) and viral (orange) proteins for three independent replicates.

(L) Fraction of viral protein intensities in total proteomic data in three replicates summarising the data shown in I-K. Bars represent the proportion of viral proteins

enriched relative to input proteins across different experimental setups. Enriched samples are indicated as en, and input as in.

(M) Fraction of viral-viral/viral-host and host-host protein pairs across three replicates.

(N) Fraction of viral-viral/viral-host and host-host interlinks across three replicates.

(O) Fraction of viral-viral/viral-host and host-host intralinks across three replicates.

(P) Venn-diagram depicting overlap of all protein pairs (above) and viral-viral/viral host protein pairs among three replicates.

(Q) Venn-diagram depicting overlap of all interlinks (above) and viral-viral/viral host interlinks among three replicates.

(R) Venn-diagram depicting overlap of all intralinks (above) and viral-viral/viral host intralinks among three replicates.

Table S1. Cross-linking data set.

(A) Cross-links filtered at 2% residue-pair FDR level

(B) Protein pairs filtered at 2% protein-pair FDR level

(C) Cross-linking data filtered at both 2% residue-pair and protein-pair FDR level

(D) Virus-centric network containing cross-links to viral proteins and between host proteins that cross-linked to viral proteins.

(E) Cross-links filtered at 5% residue-pair FDR level

(F) Protein pairs filtered at 5% protein-pair FDR level

(G) Cross-linking data filtered at both 5% residue-pair and protein-pair FDR level

Table S2. Protein pairs identified as PPIs in previous focused IAV studies.

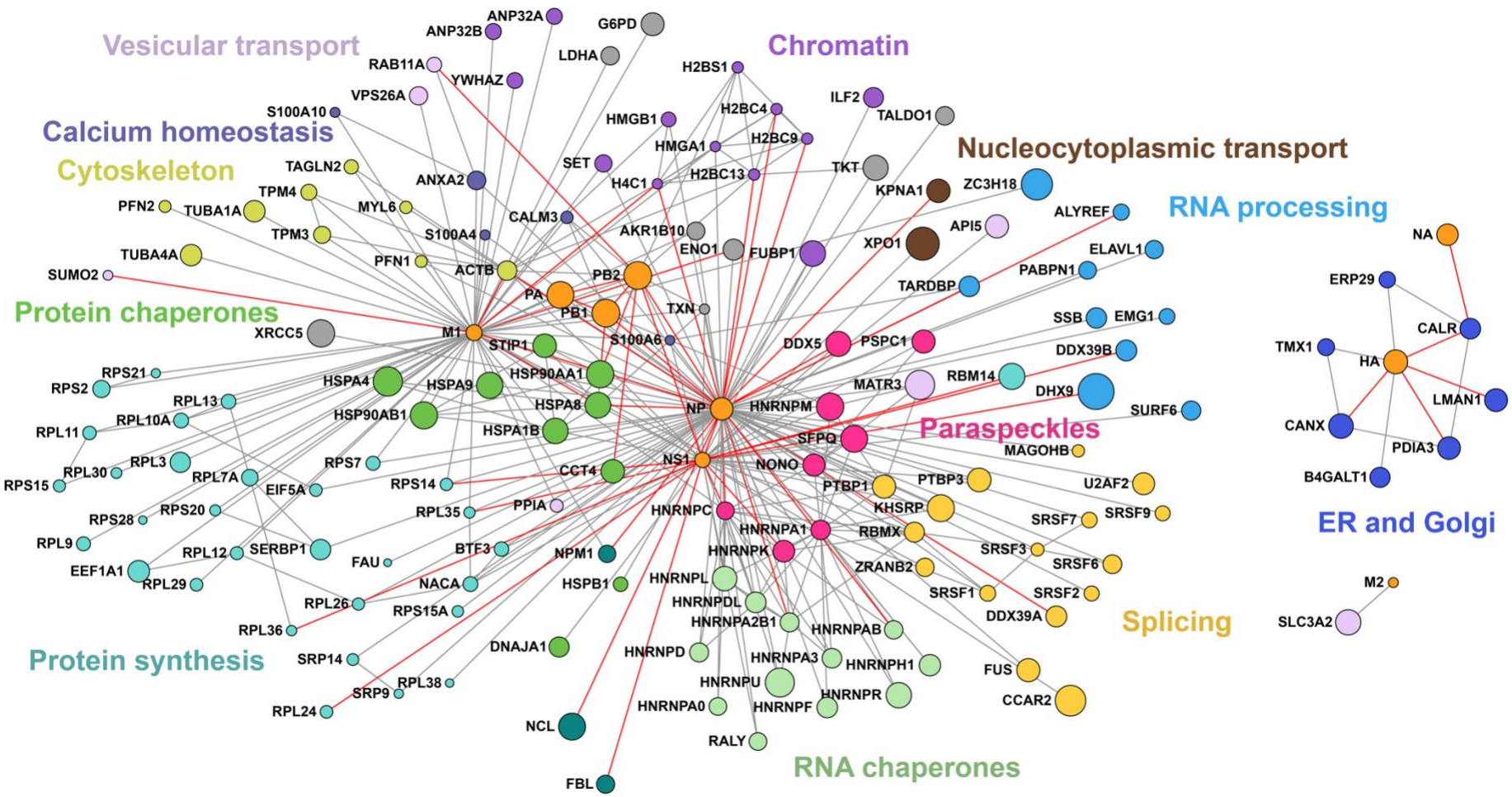

Figure S2. Cross-linking network derived at an FDR threshold of 2% at both residue- and protein-pair levels with additional information mapped.

(A) Cross-linking network highlighting known PPIs with red lines. Host proteins not linked to viral proteins are not shown for clarity. Viral proteins are shown in orange, host proteins are coloured according to the functional category as in Figure 1.

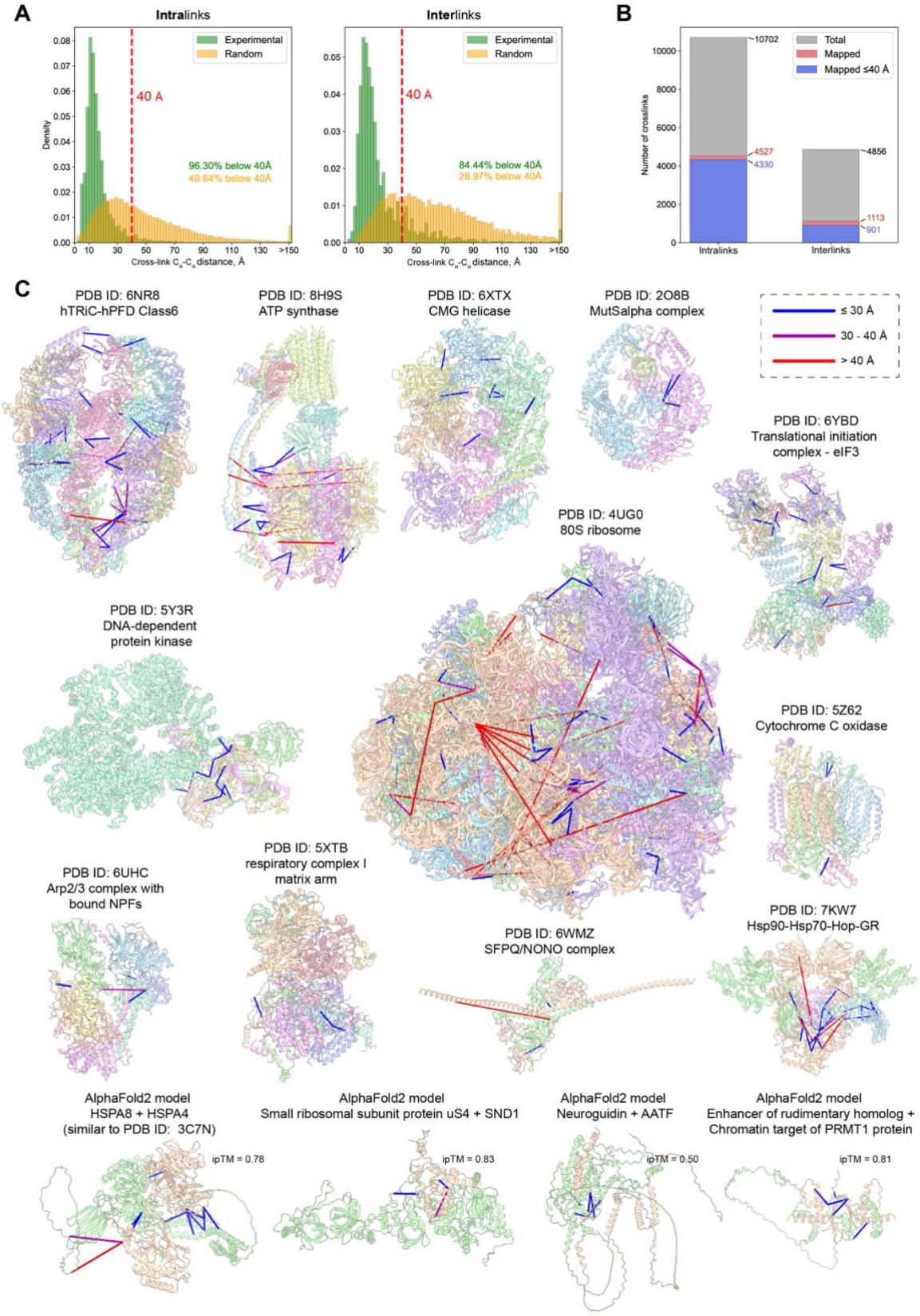

Figure S3. Validation of XL-MS data by available 3D structures and AlphaFold models of cross-linked host PPIs.

(A) Distance histogram of cross-link lengths mapped to 3D structures and AlphaFold. Random distribution corresponds to a random sample of all lysine-residue pairs. The red dashed line indicates the 40 Å threshold.

(B) Bar diagram showing the total number of inter- and intra-cross-links (gray), how many of them could be successfully mapped to PDB structures (red) and how many satisfy the Cα -Cα

(C) Satisfied cross-links (Cα-Cα distance lower than 30 Å) are coloured blue, cross-links in the range from 30 Å to 40 Å are coloured magenta, while cross-links longer than that are coloured red.

(D) Example AlphaFold2-multimer models with cross-links mapped and coloured as in (C).

Table S3. Functional enrichment analysis.

(A) Host proteins cross-linked to viral proteins and used for the enrichment analysis

(B) Enriched Reactome Pathways

(C) Enriched GO biological processes

(D) Enriched GO cellular components

(E) Enriched GO molecular functions

(F) Proteins simultaneously enriched among the host proteins in the NONO AP-MS under mock conditions and NP AP-MS infected. See also Figure 7H.

(G) GO biological processes simultaneously enriched for proteins in (F). See also Figure 7I.

Table S4. Scores of structural models of IAV-human proteins pairs modelled using AlphaFold.

(A) Models built using AlphaFold 3

(B) Models built using AF3x and all cross-links

(C) Models built using AF3x and one cross-link at a time

(D) Models built using AlphaFold 2

(E) Selected models built using AlphaFold 3 run 1,000 times with different random generator seeds

(F) Selected models built using AF3x, one cross-link, and run 1,000 times with different random generator seeds

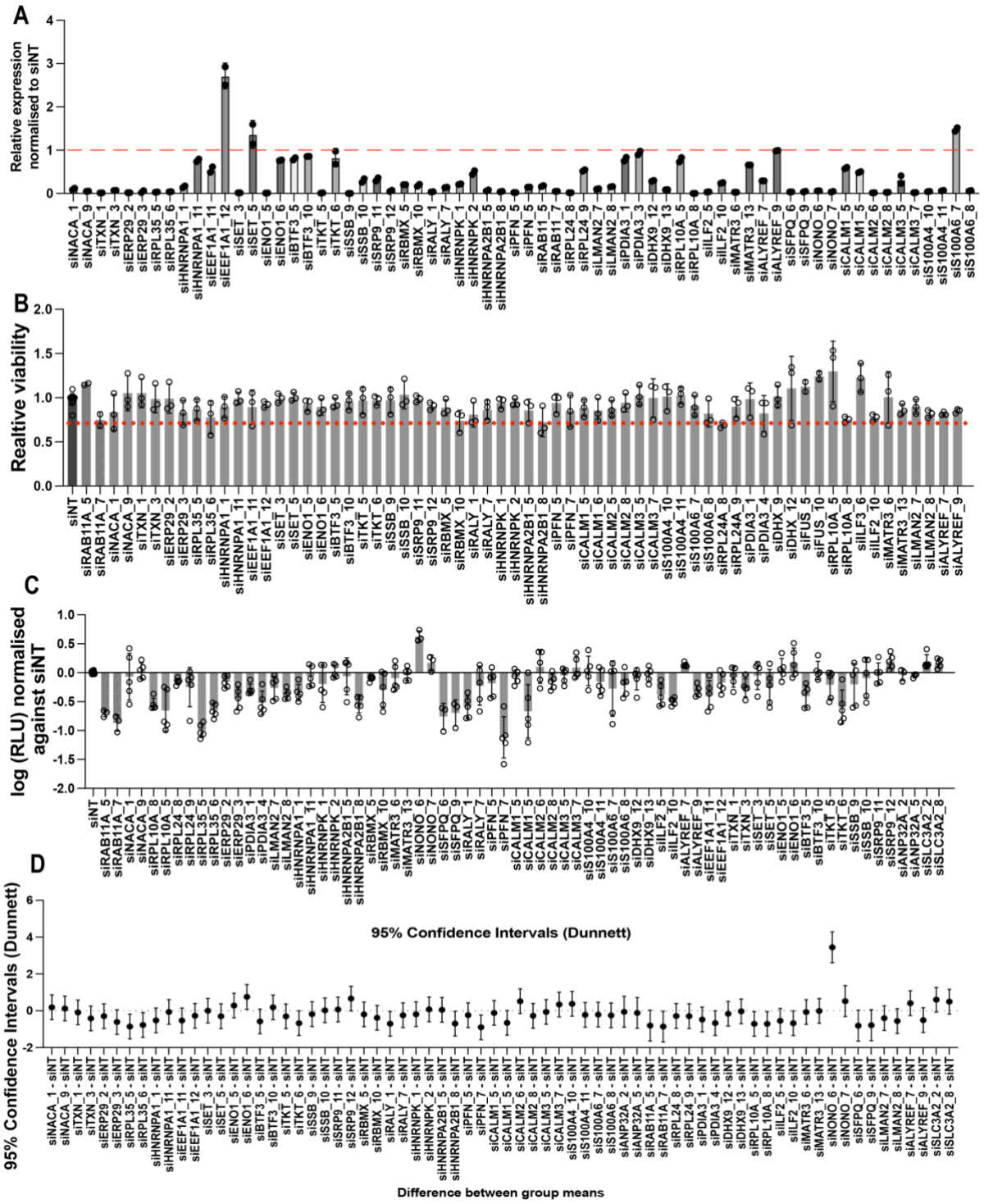

Figure S4. The results of the siRNA screen.

A) Knockdown efficiency of target genes in A549 cells using siRNA. Efficiency was assessed by qPCR. Data is represented as relative expression of target gene

normalised to the non-targeting control (siNT) (n=3). The dashed red line indicates the value obtained for the control.

(B) Viability was measured using the CellTiter-Glo assay and normalised to the non-targeting control (n = 3). The red dashed line indicates a 70% viability cut-off; siRNAs below this threshold were excluded from further analysis.

(C) Luciferase assay in A549 cells with target gene knockdown, infected with recombinant WSN (MOI 0.01, PB2-T2A-NanoLuc) for 48 h. Data are normalised to siNT (n = 4). Error bars represent mean ± SD, with significance determined by ANOVA (Dunnett's test).

(D) Confidence interval (CI) plot for luciferase activity showing comparisons between knockdowns and siNT. CIs were calculated using ANOVA (Dunnett's test, n = 4). Data are presented as mean ± 95% CI.

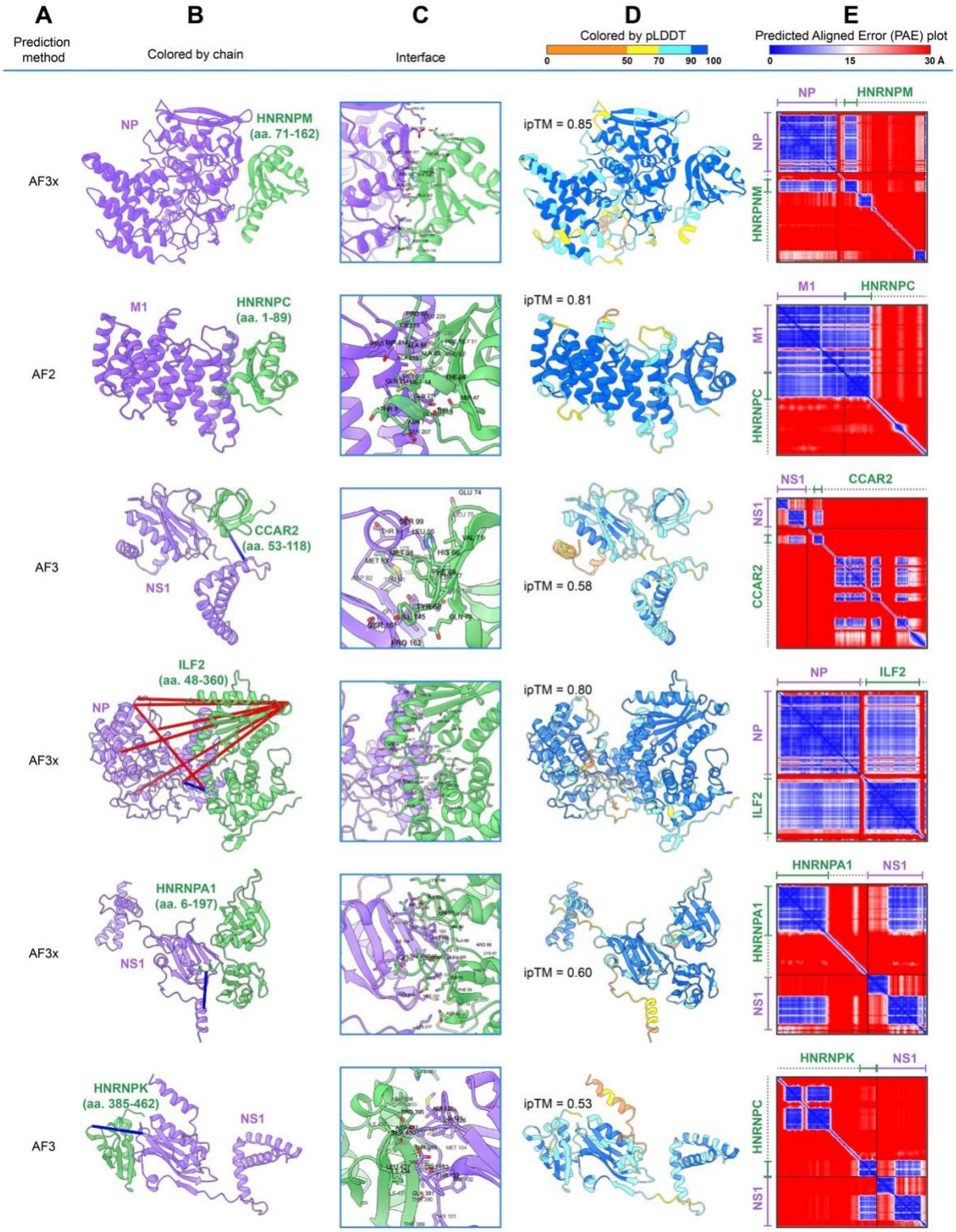

Figure S5. Structural models of IAV proteins in complex with human proteins.

Each row presents the structural model of one of the following protein pairs: NP - HNRNPM, M1 - HNRNPC, NS1 - CCAR2, NP - ILF2, NS1 - HNRNPA1, and NS1 - HNRNPK.

(A) The method used for model generation: AlphaFold2-Multimer (AF2), AlphaFold3 (AF3), and AF3x.

(B) Models, where the purple chain corresponds to the IAV protein and the green chain to the human protein. For human proteins, only fragments that confidently interact with the pathogen protein are included. The range of visible amino acids (aa.) is annotated as the first to the last residue shown. Identified interchain cross-links, if present for the shown protein fragments, are marked with lines. Cross-links satisfying the Cα-Cα distance threshold (<30 Å) are coloured blue, while longer cross-links are coloured red.

(C) Close up views on interaction sites, with residues shown that have van der Waals radius intersections greater than 0.4 Å with residues from another chain.

(D) Models coloured according to the predicted local distance difference test (pLDDT), reflecting confidence in the predicted residues (higher values indicate greater confidence). The interface predicted template modelling (ipTM) score is also indicated.

(E) Predicted aligned error (PAE) heat maps, where both axes represent residues from the N-terminus to the C-terminus (left to right and top to bottom). The colour of each matrix position represents the confidence in the spatial arrangement of residues relative to one another, with lower errors (blue) indicating higher confidence. Axes parts corresponding to the model chains are coloured to match the chain colouring in the second column. Residues of the host protein hidden from view in panels B and D are indicated by dashed lines.

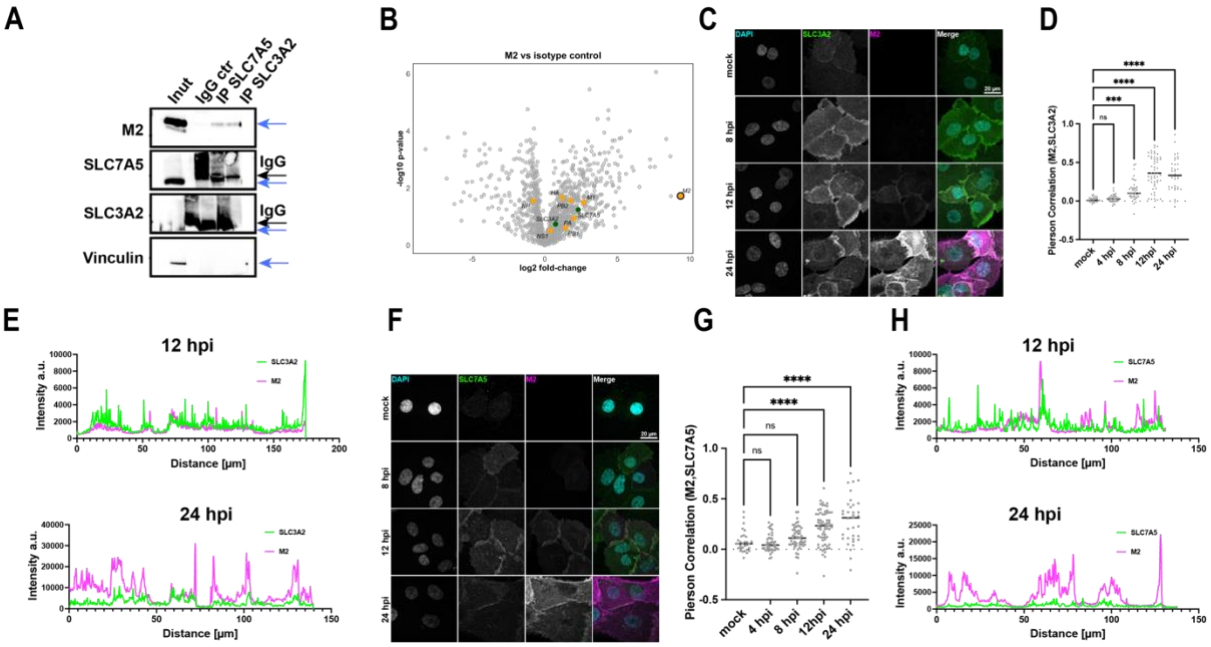

Figure S6. LAT1 in IAV infection.

(A) IP of SLC7A5 and SLC3A2 in A549 cells infected with WSN (MOI 3, 14 hpi) using antibodies against SLC7A5 and SLC3A2 or an isotype control (IgG ctr). Immunoprecipitants were analysed by Western blot for M2, SLC7A5, SLC3A2, and vinculin (negative control). Blue arrows indicate protein of interest, black ones – IgG.

(B) Volcano plots showing fold-change (log2) versus significance (-log10 p-value) for M2 versus isotype control. Viral proteins are depicted in orange, SLC7A5 and SLC3A2 – in green.

(C) Maximum intensity projection of HBEpCs cells showing colocalisation of SLC3A2 (green) and M2 (magenta). Images were taken at different timepoints during infection and show the distribution of SLC3A2 and M2 in the cells. The maximum intensity projection was generated from z-stacks to visualise overall protein localisation.

(D) Pearson correlation coefficient between SLC3A2 and M2 in both the membrane and cytoplasm of HBEpCs cells. Correlation was calculated to assess the degree of colocalisation between these two proteins using Cell Profiler with 15 % threshold.

(E) Intensity profile of a representative plane showing the localisation of SLC3A2 and M2 in several HBEpCs cells at 12 and 24 hpi. The profile represents the fluorescence intensity across a cross-section of the cells.

(F) Maximum intensity projection of HBEpCs cells showing colocalisation of SLC7A5 (green) and M2 (magenta). Images were taken at different timepoints during infection and show the distribution of SLC7A5 and M2 in the cells. The maximum intensity projection was generated from z-stacks to visualise overall protein localisation.

(G) Pearson correlation coefficient between SLC7A5 and M2 in both the membrane and cytoplasm of HBEpCs cells. Correlation was calculated to assess the degree of colocalisation between these two proteins using Cell Profiler with 15 % threshold.

(H) Intensity profile of a representative plane showing the localisation of SLC7A5 and M2 in several HBEpCs cells at 12 and 24 hpi. The profile represents the fluorescence intensity across a cross-section of the cells.

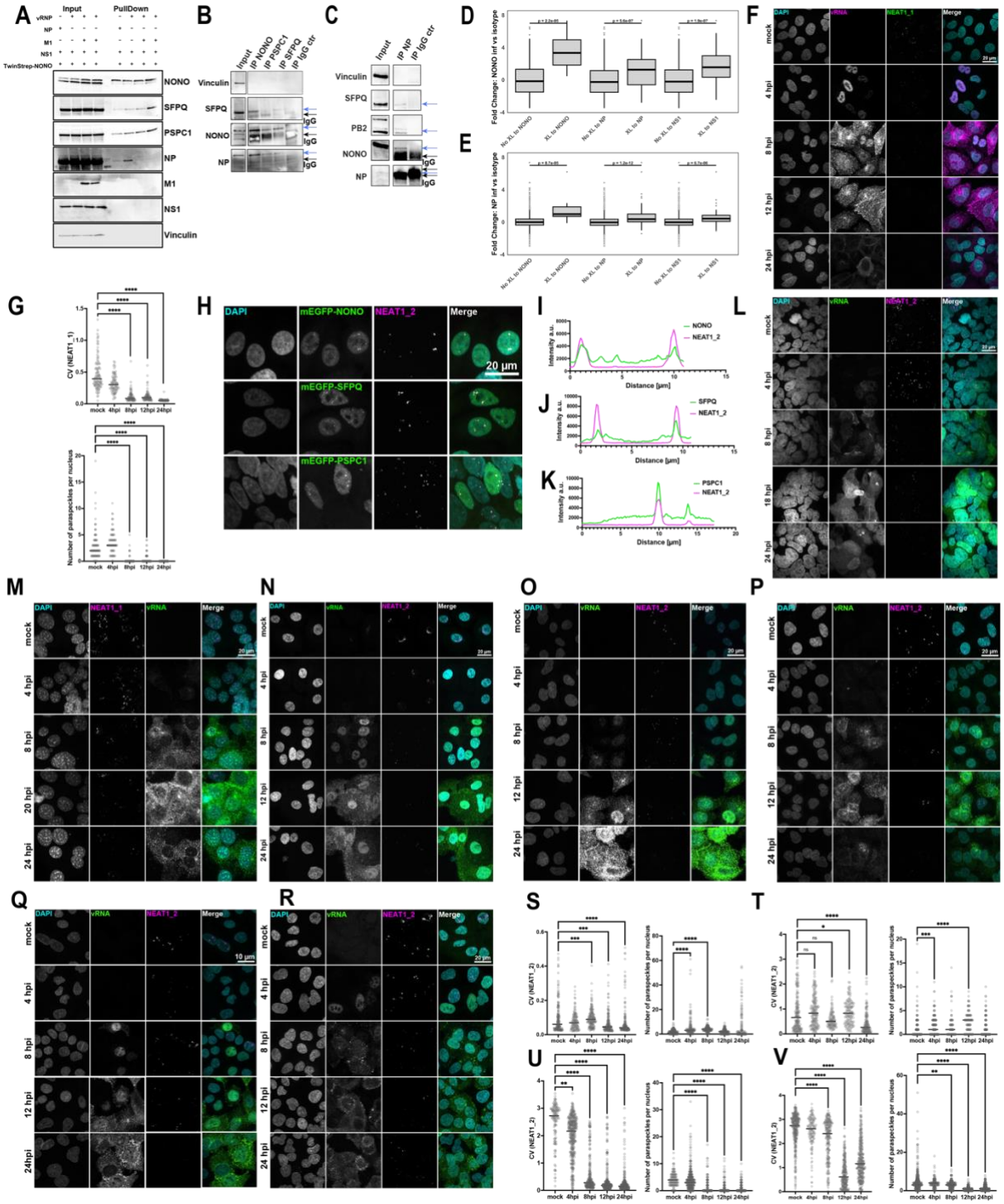

Figure S7. Analysis of paraspeckles during IAV infection.

(A) TwinStrep-tagged NONO was overexpressed in HEK 293T cells alongside the viral proteins NP, M1, and NS1, or the vRNP complex for 24 hours. Streptactin beads were used for pull-down to isolate the TwinStrep-NONO complex. Input and pull-down samples were analysed by western blot. Antibodies against NONO, SFPQ, and PSPC1 were used to confirm successful pulldown of paraspeckle proteins. Antibodies

against viral proteins NP, M1, and NS1 were employed to assess their interaction with the NONO complex.

(B) Immunoprecipitation of paraspeckle proteins NONO, SFPQ and PSPC1 and IgG control in A549 infected cells (WSN, MOI=3, 14 hpi). The proteins of interest are annotated with the blue arrows and the IgG bands with the black ones. Vinculin was used as a negative control.

(C) Immunoprecipitation of NP and IgG control in A549 infected cells (WSN, MOI=3, 14 hpi). The proteins of interest are annotated with the blue arrows and the IgG bands with the black ones. NP levels are not distinguishable from IgG bands, therefore PB2 was used as a positive control for IP. Vinculin was used as a negative control.

(D) AP-MS analysis of NONO vs. isotype in A549 cells (WSN, MOI=3, 14 hpi) control showing fold changes for enrichment of NONO, NP, and NS1 cross-linked partners identified in SHVIP, and those not cross-linked (n=3). Statistical analysis was performed using the Wilcoxon test in R. Significance levels: ***$p < 0.001$, **$p < 0.01$, *$p < 0.05$

(E) AP-MS analysis of NP vs. isotype in A549 cells (WSN, MOI=3, 14 hpi) control showing fold changes for enrichment of NONO, NP, and NS1 cross-linked partners identified in SHVIP, and those not cross-linked (n=3). Statistical analysis was performed using the Wilcoxon test in R. Significance levels: ***$p < 0.001$, **$p < 0.01$, *$p < 0.05$

(F) Representative maximum projection of confocal images showing NEAT1_1 (green), vRNA (magenta), and DAPI (cyan) staining in mock and infected A549 cells at 4, 8, 12, and 24 hpi. Scale bar = 20 µm.

(G) CV of NEAT1_1 signal intensity and the number of paraspeckles per nucleus across different time points post-infection.

(H) Maximum projection images of confocal images of lentiviral cell lines expressing mEGFP-tagged SFPQ, NONO, or PSPC1, and their colocalisation with NEAT1_2 (magenta). Scale bar = 20 µm.

(I-K) Line profiles of colocalisation: Gray value intensity profiles of NEAT1_2 (magenta) and mEGFP-tagged proteins (green) showing colocalisation across distance (in microns). (G) NONO, (H) SFPQ, and (I) PSPC1.

(L-N) Representative maximum projection of confocal images showing NEAT1_2 (magenta), vRNA (green), and DAPI (cyan) staining in mock and infected Calu-3 (L), MEFs (M), HEBpC (N) cells infected with WSN at 4, 8, 18, and 24 hpi. Scale bar = 20 μm.

(O-P) Representative maximum projection of confocal images showing NEAT1_2 (magenta), vRNA (green), and DAPI (cyan) staining in mock and infected A549 (O), HEBpC (P) cells infected with pdm09 at 4, 8, 18, and 24 hpi. Scale bar = 20 μm.

(Q-R) Representative maximum projection of confocal images showing NEAT1_2 (magenta), vRNA (green), and DAPI (cyan) staining in mock and infected A549 (Q), HEBpC (R) cells infected with H3N2/Aichi at 4, 8, 18, and 24 hpi. Scale bar = 20 μm.

(S) CV of NEAT1_2 signal intensity and the number of paraspeckles per nucleus in A549 cells during pdm09 infection at various time points.

(T) CV of NEAT1_2 signal intensity and the number of paraspeckles per nucleus in HBEpC cells during pdm09 infection at various time points.

(U) CV of NEAT1_2 signal intensity and the number of paraspeckles per nucleus in A549 cells during H3N2/Aichi infection at various time points.

(V) CV of NEAT1_2 signal intensity and the number of paraspeckles per nucleus in HBEpC cells during H3N2/Aichi infection at various time points.

Data from panels (G, S-V) are shown as individual values. Statistical analysis was performed using one-way ANOVA with Dunnett's multiple comparisons test. Significance levels: *$p < 0.05$, **$p < 0.01$, ***$p < 0.001$, ****$p < 0.0001$*.

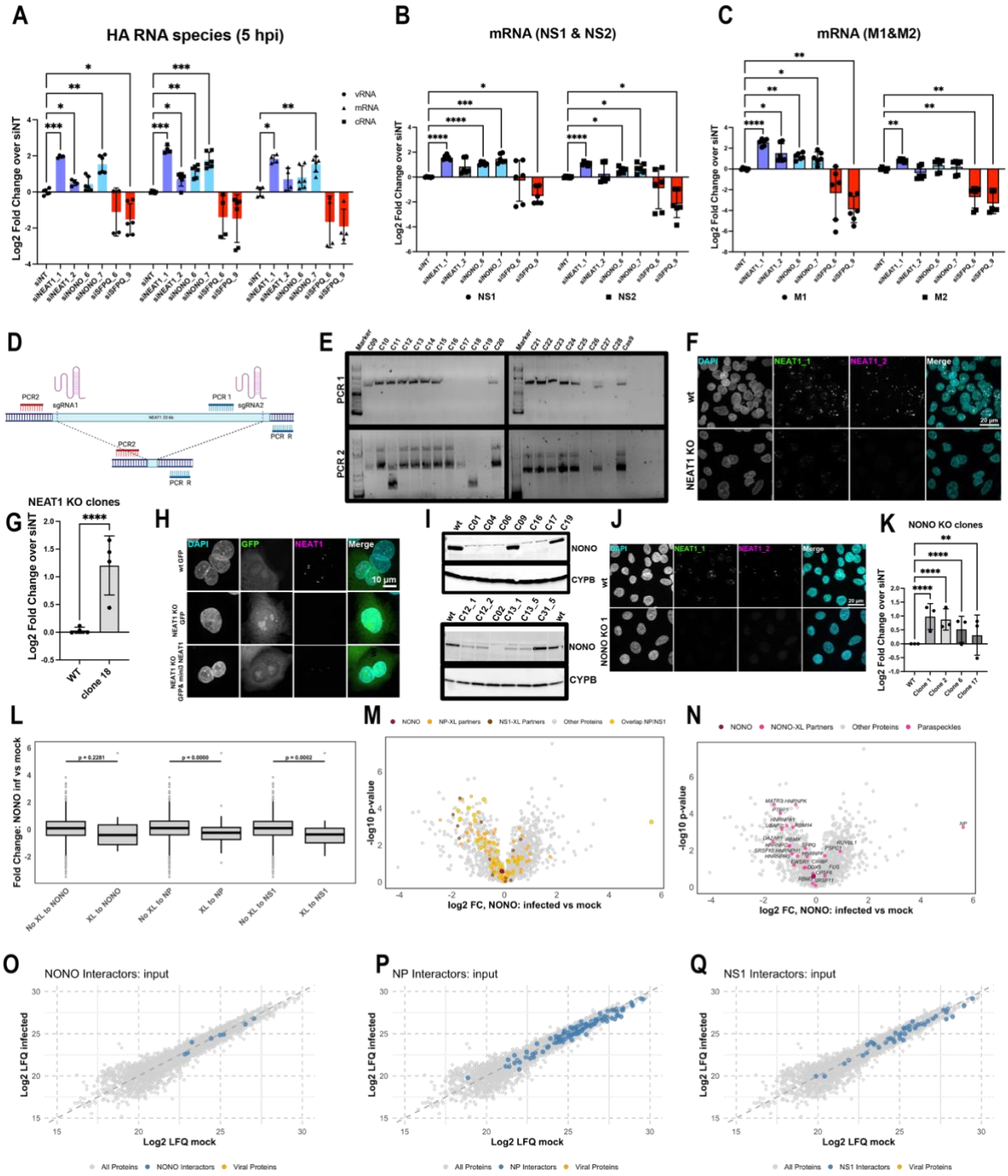

Figure S8. Role of NEAT1 and NONO during IAV infection.

(A) qPCR analysis of viral RNA species of HA fragment normalised to GAPDH in A549 cells with knockdowns of paraspeckle proteins (WSN, MOI 3, 6hpi).

(B-C) qPCR analysis of spliced and unspliced viral RNA species in A549 cells with knockdowns of paraspeckle proteins (WSN, MOI 3, 6hpi): NS, NS2 (B) and M1, M2 (C).

(D) Strategy for NEAT1 KO Generation: Schematic of the CRISPR/Cas9-based approach to generate NEAT1 KO in A549 cells. Two sgRNAs are used to target NEAT1. PCR1 amplifies the region only in wild type (WT) or heterozygous clones, whereas PCR2 detects the shorter product (approximately 500 bp) in KO clones. For heterozygous clones, both the shorter KO product and the long (23 kb) WT product may appear. *Created in BioRender. https://BioRender.com/j78u936.*

(E) PCR Screening of Clones: Agarose gel showing PCR1 and PCR2 results for various clones. Clone 18 exhibits only the shorter PCR2 product, indicating a homozygous NEAT1 KO, while Clone 11 shows both products, indicating heterozygosity.

(F) Maximum projection of confocal images of NEAT1: Representative images showing the localisation of NEAT1_1 (green) and NEAT1_2 (magenta) in WT and NEAT1 KO (Clone 28) cells. DAPI (cyan) counterstain nuclei. Scale bar = 20 µm.

(G) Quantification of luciferase activity in WT and NEAT1 KO cells.

(H) Overexpression of miniNEAT1 3 in A549 NEAT1 KO cells using electroporation partially rescued paraspeckle formation.

(I) Western blot showing NONO protein levels in WT and NONO KO clones generated using sgRNA1 (above) sgRNA2 (below). CYPB serves as a loading control.

(J) Maximum projection of confocal images of NEAT1: IF images of NEAT1_1 (green) and NEAT1_2 (magenta) in WT and NONO KO (Clone 2) cells. DAPI (cyan) counterstains nuclei. Scale bar = 20 µm.

(K) Quantification of luciferase activity in WT and NONO KO A549 cells.

(L) Fold-change in NONO AP_MS (infected vs. mock) identified in AP-MS, including NONO, NP, and NS1 cross-linked partners. Data represent mean ± SD (n = 3). Statistical significance was determined using a Wilcoxon test.

(M) Volcano plot showing fold-change (log2 FC) vs. statistical significance (-log10 p-value) of NONO AP-MS in infected vs. mock samples. Paraspeckle proteins and NONO cross-linked partners are highlighted in pink.

(N) Volcano plot showing fold-change (log2 FC) vs. statistical significance (-log10 p-value) of NONO AP-MS in infected vs. mock samples. NP-XL, NS1-XL, and overlapping interactors are colour-coded.

(O-Q) Scatter plots of Log2 LFQ values comparing infected and mock input samples in AP-MS (NONO inf and NONO mock). (O) NONO XL-partners, **(**P) NP XL-partners, and (Q) NS1 XL-partners are highlighted in blue.

Data from panels (A-C,G,K) represent mean ± SD (n = 3). Statistical analysis was performed using the one-way ANNOVA with Dunnett multiple comparison adjustment. Significance levels: ***$p < 0.001$, **$p < 0.01$, *$p < 0.05$, ns = not significant.